

Time-series high-resolution spectroscopy and photometry of ϵ Aurigae from 2006–2013: another brick in the wall*

K. G. Strassmeier^{1**}, M. Weber¹, T. Granzer¹, L. Schanne², J. Bartus^{3,1} and I. Ilyin¹



¹ Leibniz-Institute for Astrophysics Potsdam (AIP), An der Sternwarte 16, D-14482 Potsdam, Germany

² Observatory for Stellar Spectroscopy Völklingen, Hohlstrasse 19, D-66333 Völklingen, Germany

³ Konkoly Observatory MTA CsFK, Konkoly Thege M. u. 15/17, H-1121 Budapest, Hungary

Received 2014, accepted 2014

Published online 2014

Key words Stars: ϵ Aur, binaries: spectroscopic, binaries: eclipsing, stars: fundamental parameters, stars: late-type, stars: disks, techniques: radial velocities, techniques: photometry, pulsation

We present continuous and time-resolved $R=55,000$ optical echelle spectroscopy of ϵ Aurigae from 2006–2013. Data were taken with the STELLA Echelle Spectrograph of the robotic STELLA facility at the Observatorio del Teide in Tenerife. Contemporaneous photometry with the Automatic Photoelectric Telescopes at Fairborn Observatory in Arizona is presented for the years 1996–2013. Spectroscopic observations started three years prior to the photometric eclipse and are still ongoing. A total of 474 high-resolution echelle spectra are analyzed and made available in this paper. We identify 368 absorption lines of which 161 lines show the characteristic sharp disk lines during eclipse. Another 207 spectral lines appeared nearly unaffected by the eclipse. From spectrum synthesis, we obtained the supergiant atmospheric parameters $T_{\text{eff}}=7395\pm 70$ K, $\log g \approx 1$, and $[\text{Fe}/\text{H}]=+0.02\pm 0.2$ with $\xi_t=9$ km s⁻¹, $\zeta_{\text{RT}}=13$ km s⁻¹, and $v \sin i=28\pm 3$ km s⁻¹. The residual average line broadening expressed in km s⁻¹ varies with a period of 62.6 ± 0.7 d, in particular at egress and after the eclipse. Two-dimensional line-profile periodograms show several periods, the strongest with ≈ 110 d evident in optically thin lines as well as in the Balmer lines. Center-of-intensity weighted radial velocities of individual spectral lines also show the 110-d period but, again, additional shorter and longer periods are evident and are different in the Balmer lines. The two main spectroscopic H α periods, ≈ 116 d from the line core and ≈ 150 d from the center-of-intensity radial velocities, appear at 102 d and 139 d in the photometry. The H β and Johnson VI photometry on the other hand shows two well-defined and phase-coherent periods of 77 d and 132 d. We conclude that H α is contaminated by changes in the circumstellar environment while the H β and VI photometry stems predominantly from the non radial pulsations of the F0 supergiant. We isolate the disk-rotation profile from 61 absorption lines and found that low disk eccentricity generally relates to low disk rotational velocity (but not always) while high disk eccentricity always relates to high velocity. There is also the general trend that the disk-absorption in spectral lines with higher excitation potential comes from disk regions with higher eccentricity and thus also with higher rotational velocity. The dependency on transition probability is more complex and shows a bi-modal trend. The outskirts of the disk is distributed asymmetrically around the disk and appears to have been built up mostly in a tail along the orbit behind the secondary. Our data show that this tail continues to eclipse the F0 Iab primary star even two years after the end of the photometric eclipse. High-resolution spectra were also taken of the other, bona-fide, visual-binary components of ϵ Aur (ADS 3605BCDE). Only the C-component, a K3–4-giant, appears at the same distance than ϵ Aur but its radial velocity is in disagreement with a bound orbit. The other components are a nearby (≈ 7 pc) cool DA white dwarf, a G8 dwarf, and a B9 supergiant, and not related to ϵ Aur. The cool white dwarf shows strong DIB lines that suggest the existence of a debris disk around this star.



© 2014 WILEY-VCH Verlag GmbH & Co. KGaA, Weinheim

1 Introduction

Epsilon Aurigae is a single-lined (SB1) spectroscopic and eclipsing binary system with a two year long eclipse every 27.1 years (Vogel 1903, Ludendorff 1903). The system is unique in many respects. It is the brightest eclipsing binary in the sky and has the longest orbital period known among any of the eclipsing binaries. It is composed of a pulsating F0 Iab supergiant in orbit with an unseen but massive upper main sequence star that is enshrouded in a dusty

disk. The recent eclipse took place in 2009–2011 and a suite of modern instrumentation was pointed to this star for the first time. Most notably, interferometric imaging with the CHARA array resolved the opaque dusty disk in front of the F0 star during eclipse (Kloppenborg et al. 2010, Mourard et al. 2012). Too numerous is the literature on ϵ Aur to be cited here but we refer the reader to the recent summaries by Stefanik et al. (2010), Stencel et al. (2011), Chadima et al. (2011) and Harmanec et al. (2013) and the many citations therein.

The mass function from the SB1 orbit allows a high-mass and a low-mass solution. In the high-mass solution even the (unseen) secondary mass is in excess of 10 solar masses and consequently was suspected to be a stellar black

* Based on data obtained with the STELLA robotic telescopes in Tenerife, an AIP facility jointly operated with IAC, and the Automatic Photoelectric Telescopes in Arizona, jointly operated with Fairborn Observatory.

** Corresponding author. e-mail: kstrassmeier@aip.de

hole (Cameron 1971, Wilson 1971). However, the lack of X-ray emission (e.g. Wolk et al. 2010) at the optical position of the secondary makes a black-hole scenario unlikely. The disk would then be a young proto-planetary system. In the low-mass scenario the secondary mass would be 3–6 M_{\odot} according to a B main-sequence star. If so, the disk would then be an accretion disk with material from the now less-massive F0 supergiant that would be in a post-asymptotic giant branch stage. New orbital elements were presented just recently by Stefanik et al. (2010) and Chadima et al. (2010) from radial velocities covering over 100 years and constrain the mass function to 2.51 ± 0.12 . However, both studies again did not detect spectral lines from the secondary star itself and thus can not decide between the two scenarios.

The decision of which scenario is the correct one is plagued by the uncertain distance of ϵ Aur along with the fact that most stellar parameters are also uncertain. The nominal *Hipparcos* value of 650 pc (van Leeuwen 2007) has errors that allows a distance between 350 pc and more than 4 kpc. Earlier astrometric distances are in agreement with this nominal value but with much smaller errors. Heintz & Cantor (1994) obtained 606 ± 60 pc while van de Kamp (1978) obtained 580 ± 30 pc. Note that the errors of the van de Kamp value from Sproul-refractor plates were most likely underestimated because their positional and photometric elements did not agree with each other. However, a recent redetermination (Guinan et al. 2012) of the interstellar absorption towards ϵ Aur places the system out to 1.5 ± 0.5 kpc, which would favor the high-mass scenario.

Spectroscopic studies during the eclipse 1982–1984 showed remarkable changes in some absorption lines during eclipse (Lambert & Sawyer 1986). In particular, large changes in line profiles and equivalent widths were seen in the Balmer lines and in the resonance lines K I 7699 and the Na D doublet due to additional Doppler shifted absorption components. These influences are caused by the gas surrounding the opaque dusty disk. New medium-resolution optical spectroscopy from the most recent eclipse still did not detect the B star that must be deeply enshrouded in the disk (Chadima et al. 2011). *Herschel* observations confirmed the cool temperature of the disk of 550 K (Hoard et al. 2012) while earlier IR observations revealed 1150 K when that part of the disk was seen that faces the F supergiant, possibly due to a heating effect from the F star. The lack of strong molecular emission features from the disk is suggestive of a low gas-to-dust ratio. In a recent paper based on optical spectroscopy dating back to the 1930s, Griffin & Stencel (2013) presented evidence for a confined mass stream from the F0 primary to the unseen secondary.

Photometric studies date back to 1842 (Ludendorff 1903; see the literature summary in Stefanik et al. 2010). Out-of-eclipse variations were noticed all along but only recently was its multi-periodic nature discovered (Kim 2008, Kloppenborg et al. 2012). The presence of two drifting periods of on average 67 d and 123 d (Kim 2008),

but between 52 d to 217 d as a function of time (Kloppenborg et al. 2012), suggest that the F supergiant is a complex multi-periodic non-radial pulsator.

In this paper, we present and analyze our own new optical photometry and spectroscopy of ϵ Aur. We employed our robotic telescopes STELLA (actually two telescopes) in Tenerife and the Amadeus-APT in Arizona. The STELLA echelle data, acquired between 2006 and 2013, are used to study the disk-gas absorption lines during the eclipse and to compare the behavior between inside and outside of eclipse. The goal is to learn more about the ϵ Aur F-supergiant and to shed some light on the physical conditions within the gaseous volume of the disk. The paper is structured as follows. Section 2 presents the new data and describes the instruments. Sect. 3 analyses the global atmospheric parameters and presents a phenomenological description of the optical spectra of ϵ Aur. Sect. 4 focuses on the rotation of the F supergiant. Sect. 5 attempts to analyze the line-profile variability presumably caused by excited surface oscillations and a stellar wind. Sect. 6 presents and analyzes the APT photometry and Sect. 7 investigates the multiple stars system around ϵ Aur = ADS 3605A. Sect. 8 is our summary. For orientation, note that the time span of the photometric eclipse was from 1st contact at JD 2,455,070 \pm 10 (August 2009) to 4th contact at JD 2,455,800 \pm 14 (May 2011) according to Chadima et al. (2011).

2 New observations and data reductions

2.1 High-resolution optical spectroscopy 2006–2013

Time-series high-resolution echelle spectroscopy was obtained with the 1.2 m STELLA telescopes between September 19, 2006 and Dec. 4, 2013 (and continuing). A total of 474 spectra of ϵ Aur were obtained over the course of almost 7 years. The bulk of the spectra were taken with an exposure time of 120 s and achieved a signal-to-noise (S/N) ratio of between 100–400:1 per resolution element. Some spectra were exposed longer to reach a S/N ratio of up to 500:1 but many had S/N below 100:1 due to clouds and bad weather. Several Morgan-Keenan (MK) standard stars were observed randomly in time, among those are ϕ 34 Cas (F0Ia), α 11 Lep (F0Ib), HD 10494 (F5Ia), α 33 Per (F5Ib), HR 825 = V480 Per (A5Ia), HR 2874 (A5Ib), and 32 Gem (A9III). A portion of a representative spectrum of ϵ Aur during egress is compared with two of above MK-standard stars in Fig. 1.

STELLA-I is a fully robotic telescope that, together with STELLA-II, makes up the STELLA observatory of the AIP at the Izãna ridge on Tenerife in the Canary islands (Strassmeier et al. 2004, 2010). The fiber-fed STELLA Echelle Spectrograph (SES) is the telescope's only instrument. It is a white-pupil design with an R2 grating with two off-axis collimators, a prism cross disperser and a folded Schmidt camera with an e2v 2k \times 2k CCD as the detector, the latter two items until mid 2012. Spectra have a fixed

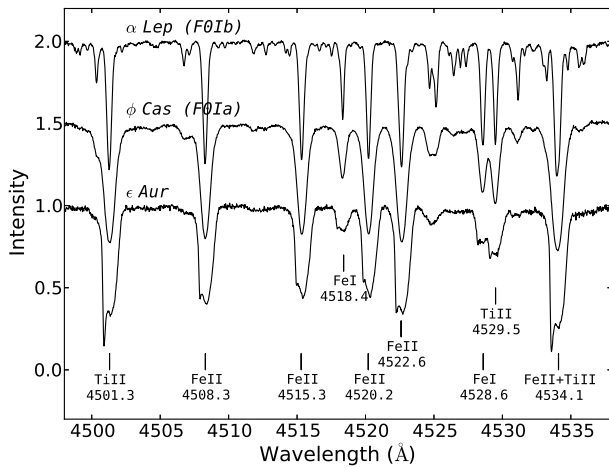


Fig. 1 A small portion of our spectra around the 4520-Å region. Shown is a comparison of a spectrum of ϵ Aur during eclipse (bottom) with the MK standard stars α Lep (top) and ϕ Cas (middle). Note the sharp blue-shifted absorption in the line profiles of ϵ Aur from the transiting disk around the unseen secondary star.

format on the CCD and covered the wavelength range from 388–882 nm with increasing inter-order gaps near the red end starting at 734 nm towards 882 nm. The SES received a major upgrade in summer 2012 with a new cross disperser, a new optical refractive camera, and a $4k \times 4k$ e2v CCD. This removed the inter-order gaps in the red. A bit earlier, the SES fiber was moved to the prime focus of the second STELLA telescope (STELLA-II). From 1.1.2012 through 30.5.2012 the off-axis parabolas were misaligned which resulted in a lowered spectral resolution for that period of time. The nominal resolving power is $R=55,000$ corresponding to a spectral resolution of 0.12 \AA at 650 nm (3-pixel sampling). An example spectrum of the entire wavelength range is shown in the appendix in Fig. A1. Further details of the performance of the system were reported by Weber et al. (2012) and Granzer et al. (2010).

Data reduction is performed automatically using the IRAF¹-based STELLA data-reduction pipeline (Weber et al. 2011). Images were corrected for bad pixels and cosmic-ray impacts. Bias levels were removed by subtracting the average overscan from each image followed by the subtraction of the mean of the (already overscan subtracted) master bias frame. The target spectra are flat fielded with a nightly master flat which has been normalized to unity. The nightly master flat itself is constructed from around 50 individual flats observed during dusk, dawn, and around midnight. After removal of the scattered light, the one-dimensional spectra were extracted with the standard IRAF optimal extraction routine. The blaze function was then removed from the target spectra, followed by a wavelength calibration using consecutively recorded Th-Ar spectra. Finally, the extracted spectral orders were continuum normalized by di-

¹ The Image Reduction and Analysis Facility is hosted by the National Optical Astronomy Observatories in Tucson, Arizona at URL iraf.noao.edu.

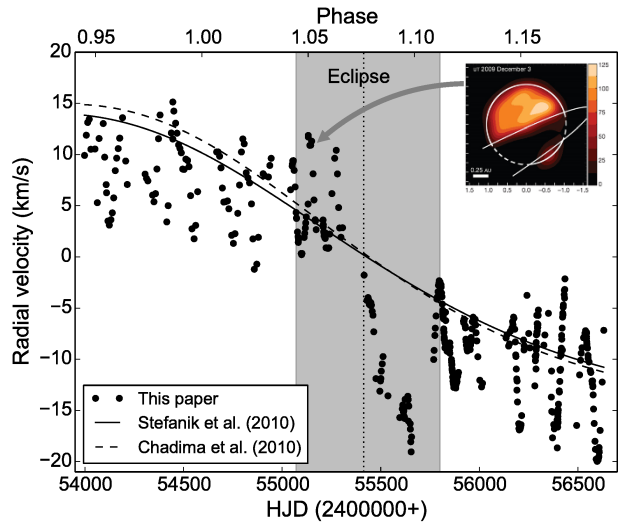


Fig. 2 STELLA radial velocities of the F0I primary of ϵ Aur (dots). The full line is the 27-year SB1 orbital solution from Stefanik et al. (2010). Orbital phases were computed from their “combined” solution. For comparison the dashed line is the orbit from Chadima et al. (2010); only their PHOEBE solution is shown but with the systemic velocity from Stefanik et al.. The gray-shaded region emphasizes the time of the photometric eclipse and the dotted vertical line marks the zero velocity of the disk-absorption lines. The graphics insert features one of the two CHARA images from Dec. 3, 2009 (Kloppenborg et al. 2010) taken during eclipse ingress.

viding them with a flux-normalized synthetic spectrum of the same spectral classification as the target in question.

Note that the external radial-velocity rms errors were significantly larger during the initial year of STELLA operation in 2006/07 ($\approx 120 \text{ m s}^{-1}$) compared to thereafter ($\approx 30 \text{ m s}^{-1}$). The final radial velocities in this paper are barycentric and corrected for Earth rotation and are given in Table 1. No gravitational redshift corrections were applied. The zero point of STELLA radial velocities is $+0.503 \text{ km s}^{-1}$ with respect to CORAVEL (see Strassmeier et al. 2012). All velocities in the present paper are on the STELLA system.

Spectra of the fainter ADS3605 components were taken with the Nordic Optical Telescope (NOT) at La Palma and its high-resolution fiber-fed echelle spectrograph FIES (Telting et al. 2013) in the time period Nov. 15–20, 2013. FIES was used in its medium-resolution mode with fiber bundle 3 ($R=47,000$) and the $2k$ e2v CCD which covered the wavelength range 365–727 nm. The data were reduced with FIESstool (see also Telting et al. 2013). Spectra are shown later in the paper in Fig. 16. STELLA-SES spectra were taken of the brightest of these stars (BD+43°1168) starting Nov. 5, 2013.

2.2 Time-series APT photometry 1996–2013

All new data were obtained with the Potsdam-Vienna *Amadeus* (T7) automatic photoelectric telescope (APT) at

Table 1 Global radial velocities for ϵ Aur.

HJD	v_r (km s ⁻¹)	rms (km s ⁻¹)
2454006.56275	11.889	0.056
2454013.57087	13.133	0.028
2454021.55185	13.449	0.000
2454029.58578	10.514	0.042
2454050.51433	10.539	0.091
2454062.46766	5.296	0.000
2454071.44339	11.568	0.000
2454092.42028	13.028	0.017

Full table available only electronically.

Fairborn Observatory in southern Arizona (Strassmeier et al. (1997). Continuous H α and H β photometry for the years 1996–2000 was presented earlier by Strassmeier et al. (2001) as part of a paper on the magnetically-active star Capella. From 2001 until 2008, the same filter in H α of 31-Å full width half maximum (FWHM) was employed as before and with the same EMI-9828 photomultiplier tube (see Strassmeier et al. 2001 for a filter description). During the initial observations in 1996/97 we also used Strömgren b, y filters on the sister telescope *Wolfgang* for a short period in time. During the observing season 1999/2000 additional time-series H β photometry on the *Wolfgang* telescope was done. After 2008, Johnson-Cousins $V(I)_C$ filters were employed instead. For the present paper, a total of 2577 new observations in H α , V , and I_C (furtherin denoted as I) were obtained. Typically, one APT observation consists of three integrations on the variable, four integrations on the comparison star, two integrations on the check star, and two integrations on a sky position. Integration times were 20 s in by , 30 s in H α and H β , and 10 s in VI . All APT data are given numerically in Table 2.

The initial 1996/97 observations of ϵ Aur used a 3.75-mag neutral-density (ND) filter which was changed to a 1.25-mag ND filter thereafter. No neutral filter was inserted for the comparison star HD 33167 = HR 1668 (F5V, $V=5^m77$) and the check star HD 34411 = HR 1729 (G2, $V=4^m70$), except in 1996/97 where a 1.25-mag ND filter was used for HD 33167.

All data were obtained through a 30'' diaphragm. The standard error of a nightly mean for *Amadeus* from the seasonal mean changed over the past decade but was typically 4–6 mmag in V and 6–8 mmag in I_C . The observing seasons between 2007–2009 showed increasing scatter due to a slowly but systematic malfunction of the acquisition CCD camera. By late 2009 it had gotten so bad that we had to exchange the entire camera plus its CCD and after that, starting with HJD 2,455,143, the performance was back to the original values quoted above. For further details we refer to Granzer et al. (2001).

From concurrent observations of Johnson standards in $V(I)_C$ in 2008–2013, we also deduce an all-sky solution and apply it to the differential values whenever feasible. Its

Table 2 Differential photometry of ϵ Aur. HJD is the barycentric JD at the mid time of the observation, Δt is the duration of the observation, X is the airmass, then come the differential magnitudes for the various bandpasses, *err* is the standard error of the mean.

HJD	Δt (s)	X	Δb (mag)	err (mag)	Δy (mag)	err (mag)
245...	514	1.19	-2.5295	0.006	-2.6642	0.006
245...	512	1.17	-2.5325	0.001	-2.6674	0.002
245...	515	1.15	-2.5349	0.001	-2.6694	0.001
245...	513	1.07	-2.5328	0.001	-2.6689	0.001
245...	512	1.06	-2.5364	0.001	-2.6679	0.001
245...	512	1.06	-2.5349	0.000	-2.6667	0.001
245...	512	1.05	-2.5347	0.001	-2.6704	0.001
245...	513	1.04	-2.5338	0.001	-2.6673	0.001

Full table available only electronically.

accuracy never significantly exceeds 0^m01 in V though. Absolute errors are also typically around 0^m01 for $\Delta(V - I_C)$ except for the bad time period 2007–2009, as mentioned above, and was then likely 0^m02. Note that in Fig. 13, we shifted the H α , H β , and b, y magnitudes arbitrarily to match the V -brightness. The shifts were determined from the seasonal averages in each filter and have uncertainties of up to $\pm 0^m04$.

3 The optical spectrum of ϵ Aurigae

3.1 Global radial velocities

Fig. 2 shows the observed velocities for the entire STELLA observing period 2006–2013. Radial velocities were determined from a simultaneous cross correlation of 62 échelle orders (excluding the Balmer lines) with a synthetic template spectrum from an ATLAS-9 atmosphere (Castelli & Kurucz 2004) matching the target spectral classification. We call these velocities global because of their disk average nature. Radial velocities from individual spectral lines are discussed later in Sect. 5. At least four, unrelated, components contribute to the global velocities. *i*) Semi-regular variations due to the F0-star pulsation. These are dominant outside of eclipse and have peak-to-valley amplitudes of between 10–15 km s⁻¹ and remain visible throughout the eclipse. *ii*) Radial velocity variations due to the eccentric binary motion. These amount to approximately 20 km s⁻¹ for the time span of our observations and are the cause of the trend seen in Fig. 2. *iii*) Radial velocity variations induced by the eclipsing body. These are due to disk rotation and due to the asymmetry caused by the missing flux from the eclipsed region on the F0 star that suppress certain pulsation modes and certain Doppler shifts of its surface rotation profile (a “Rossiter-McLaughlin” effect). Our data indicate a full drop at egress with an amplitude of 20 km s⁻¹ with respect to the orbital motion. *iv*) Selective zero-point shifts of the wavelengths of wind-sensitive lines like H α .

Table 3 Global atmospheric parameters from spectrum synthesis.

Target	MK type	T_{eff} (K)	$\log g$ (m s^{-2})	[Fe/H] (solar)	$v \sin i$	ξ_t (km s^{-1})	ζ_{RT}	N
ϵ Aur	F0Iab	7395 ± 70	1 ± 1	$+0.02 \pm 0.2$	28 ± 3	9.2 ± 0.4	13	474
<u>M-K standards:</u>								
ϕ 34 Cas	F0Ia	7400 ± 150	...	-0.1 ± 0.15	23 ± 3	7.6 ± 0.15	13	3
α 11 Lep	F0Ib	7200 ± 150	...	-0.18 ± 0.07	8 ± 1.5	3.8 ± 0.1	13	3
HD 10494	F5Ia	6875 ± 150	...	-0.17 ± 0.1	19.6 ± 1	6.7 ± 0.1	10	2
α 33 Per	F5Ib	6480 ± 300	...	-0.24 ± 0.2	12 ± 1	5.0 ± 0.3	10	2
HR 825	A5Ia	8000 ± 160	...	-0.5	30 ± 4	13.7 ± 1	13	1
HR 2874	A5Ib	8000 ± 400	...	-0.13 ± 0.6	11 ± 3	5.3 ± 1	13	2

N , number of STELLA spectra used.

There are no direct traces from the secondary star in the spectrum. If it is indeed a main-sequence B-star, we would expect quite large rotational broadening and lines would not be easily visible in a combined spectrum. We may note that our spectra show increased Balmer-line wing absorption by the end of the eclipse but still within the dusty eclipse, in particular for $H\alpha$, $H\gamma$, $H\delta$ and $H\epsilon$ although not for $H\beta$ (see Fig. A1 in the appendix). For $H\alpha$ and $H\gamma$ the wings extend $\pm 20 \text{ \AA}$ ($\approx 900 \text{ km s}^{-1}$) from the line core and could be due to the thermal broadening of a hot secondary main-sequence star. However, we see no obvious asymmetry of these wings with respect to the primary stars due to orbital radial-velocity changes, but this would be expected because the eclipse is close to the periastron passage and both components would have similar radial velocities. Harmanec et al. (2013) computed orbital elements from the $H\alpha$ emission wings and from weak symmetric absorption lines separately and found that $H\alpha$ basically follows the F star.

Figure 2 shows that the global radial velocities of the F0 primary during ingress were on average 5 km s^{-1} above the orbital velocity but 10 km s^{-1} below during egress. It suggests that the eclipsing body is significantly asymmetric and more extended than just the dust disk that causes the optical eclipse. Stefanik et al. (2010) presented two improved orbital solutions. One solution takes into account the photometric mid-eclipse timings as additional constraint (plotted in Fig. 2) while the other is solely based on the radial velocities. The pure Keplerian solution predicts that the orbital mid eclipse precedes the photometric mid eclipse by 9 months, which would indicate a very asymmetric mass distribution for the secondary, most likely due to the dusty disk. Chadima et al. (2010) also presented improved orbital solutions by using two different software packages. Fig. 2 shows the elements from the PHOEBE solution because it has somewhat smaller internal errors. No γ -velocity was given by Chadima et al. (2010) and therefore the value from Stefanik et al. (2010) was adopted. Our velocities are consistent with both solutions but may improve the orbit if included. Numerical values are given in Table 1.

3.2 Global atmospheric parameters

Synthetic spectra are fit to all individual STELLA spectra. We apply our tool PARSES (“PARAMeters from SES”; Allende-Prieto 2004). PARSES is implemented as a suite of Fortran programs within the STELLA data analysis pipeline and is based on the synthetic spectrum fitting procedure described in Allende-Prieto (2004). Synthetic spectra are computed and pre-tabulated for a large range of relative logarithmic metallicities, gravities and temperatures for a wavelength range of 380–900 nm. All calculations in this paper are based on MARCS model atmospheres (Gustafsson et al. 2008) with the VALD3 line list (Kupka et al. 2011; with updates on some specific $\log g f$ values). Radial-tangential macro-turbulence, ζ_{RT} , was tailored to the expected values for supergiants based on empirical data from Gray (2005). This grid is then used to fit 62 of the 80 échelle orders of each STELLA/SES spectrum. The five parameters T_{eff} , $\log g$, [Fe/H], $v \sin i$ and micro-turbulence ξ_t are solved for simultaneously in all échelle orders. However, the gravity for hot supergiants is outside of the model range for MARCS and was extrapolated for F0 and kept fixed for F5–A5. Internal errors are determined from the rms of the individual order solutions but external errors, in particular for the gravity, are hard to come by due to the individually different pulsation patterns of these stars.

The grand time-averaged parameters from our spectra are $T_{\text{eff}}=7395 \pm 70 \text{ K}$, $\log g \approx 1$ (with an uncertainty of at least 1 dex), and [Fe/H]= $+0.05 \pm 0.08$. The average from spectra prior to eclipse, i.e. from the first three years of STELLA data, are $T_{\text{eff}}=7405 \pm 150 \text{ K}$, $\log g \approx 1$, and [Fe/H]= $+0.06 \pm 0.08$ and for the time after eclipse, i.e. from the last year of STELLA data, are $T_{\text{eff}}=7350 \pm 60 \text{ K}$, $\log g \approx 1$, and [Fe/H]= $+0.06 \pm 0.09$. These are practically identical to the results from spectra within eclipse. Note that our $\log g$ values do not properly converge and must be prescribed. Previous determinations are available from Sadakane et al. (2010) who obtained $T_{\text{eff}}=8025 \text{ K}$, $\log g=1.0$, $\xi=10 \text{ km s}^{-1}$ and a combined macro-turbulence and rotational broadening of 27 km s^{-1} from the O I lines near 6157 \AA , all with solar metallicity. Chadima et al. (2011) qualitatively compared synthetic spectra with their own observations and found

the best match with an average out-of-eclipse spectrum at $T_{\text{eff}}=8000$ K, $\log g=1.0$, $M/H=-0.3$, and $v \sin i=5.0$ km s $^{-1}$. Stefanik et al. (2010) found the best correlation with a synthetic spectrum with 7750 K, $\log g=1.5$ and a total line broadening of 41 km s $^{-1}$ assuming solar metallicities. Most recently, Griffin & Stencel (2013) matched their blue DAO CCD spectra with a $T_{\text{eff}}=7300$ K, $\log g=0.2$, $M/H=0.0$, $\xi=10$ km s $^{-1}$, and $v \sin i=36$ km s $^{-1}$ model. It is in excellent agreement with our STELLA-PARSEs values except $v \sin i$. Griffin & Stencel (2013) gave no indication of their macroturbulence assumptions and we suspect that their “rotational broadening” is the combination of rotation and macroturbulence. We emphasize again that the inconsistent treatment of micro- and (radial-tangential) macroturbulence has a profound impact on the extracted rotational broadening (courtesy Gray 2005). Moreover, most of above previous studies had to use pulsation-averaged spectra taken at different times, and thus at different state of the oscillation. This clearly introduces an unsolvable problem for the line synthesis and results in combinations of too high an effective temperature and gravity and/or lowered metallicity.

For comparison, we apply our spectrum analysis also to STELLA spectra of the following MK standard stars; ϕ 34 Cas (F0Ia), α 11 Lep (F0Ib), HD 10494 (F5Ia), α 33 Per (F5Ib), HR 825 = V480 Per (A5Ia) and HR 2874 (A5Ib). The individual results are given in Table 3 and are in agreement with the fundamental parameters given by Kovtyukh et al. (2012) whenever available. Further results are given in Sect. 4.

3.3 Equivalent widths

We measure the equivalent widths (EW) of a total of 368 individual absorption lines as a function of time. Of these, 207 lines show no apparent influence from the eclipsing disk, at least not at the level of the S/N ratio of our spectra. These lines are identified in the Appendix in Table B1. The remaining 161 lines show the typical profile changes during photometric eclipse (JD 2,455,070 to 2,455,800). These lines are listed in the Appendix in Table B2. The nature of many of these lines were already recognized and identified in earlier papers, e.g. by Castelli (1978), Hack (1959) and Sadakane et al. (2010) but never for the full optical spectrum from 388 to 880 nm. Fig. A1 in the appendix shows two representative full STELLA spectra of ϵ Aur prior to and inside of the eclipse. Besides the effect of the disk eclipse itself, all spectral line profiles vary due to the F-star oscillations with different levels for different lines. These variations are present outside and inside of eclipse and are also manifested by temporal variations in equivalent width and central wavelength. The Balmer line profiles are additionally distorted due to an inhomogeneous wind.

EWs in milli Angstrom were measured with the Time-Series Analysis (TSA) utility in MIDAS by one of us (LS). We selected two wavelength points on each side of a spectral line to represent the continuum as close as possible and then integrated the area beneath. No functional fitting was

performed nor were lines deblended. The aim was simply to identify time variability of the line strengths. Our EWs may thus differ from Gaussian-fit based EWs and could be considered upper limits.

An outstanding line is the neutral potassium line K I at 7699 Å. The photospheric line is very weak in pre-eclipse spectra and moreover heavily masked by terrestrial lines but the disk absorption increases in strength so that the line dominates this wavelength region during eclipse. This was already noticed in the previous eclipse by Lambert & Sawyer (1986). For the recent eclipse, EW measurements by Leadbeater & Stencel (2010, 2012) suggested a step-wise increase that was interpreted to be due to a ring-like morphology of the disk, like the rings of Saturn (see also Stencel 2012). This is not confirmed by the K I observations of Potravnov & Grinin (2013) nor by our data in this paper.

It is worthy to note that we detect a very weak He I absorption at $\lambda 5875$ Å (see in Fig. 16). A Gaussian fit gives an average equivalent width of just 11.7 ± 0.4 mÅ compared to 327 mÅ for the B9Iab-star BD+43°1168 (see Sect. 7). At least this is consistent with its post-main-sequence status.

3.4 Spectral lines without disk absorption during eclipse

The following spectral lines were selected for representing the group of the 207 lines without eclipse imprint. Their origin is likely the deep photosphere of the F0 supergiant as already pointed out by Lambert & Sawyer (1986), e.g., for the nitrogen triplet. The line profiles of several unblended lines appear symmetric within the quality range of the spectra. Therefore, we did not attempt to systematically measure line bisectors. Full width at half maximum (FWHM) of these 207 lines measure between 0.4–2 Å with a temporal variability of typically $\pm 30\%$ of the respective mean due to the F-star oscillations.

3.4.1 Si II 6347, 6371

Si II 6347 and Si II 6371 are moderately strong absorption lines in the spectrum of ϵ Aur. The profile variability of the Si II 6347 line over the entire observation period is shown in Fig. 3a. We see no obvious influence on the shape of the line profile due to the eclipse, just the semi-regular shifts in wavelength of up to ± 60 km s $^{-1}$ due to the F0-star oscillation. These wavelength shifts are accompanied by irregular and unevenly spaced short-term fluctuations of about ± 5 km s $^{-1}$, indicative of an unresolved but multi-periodic oscillation pattern. Note that the binary motion has been removed in these dynamic plots. The line equivalent widths show variations of around the mean of ≈ 600 mÅ (for Si II 6347), but no transients from the eclipsing body.

3.4.2 N I 7468

Fig. A1 in the appendix shows several N I lines such as 7423, 7442, 7468, 8629, 8683, 8703, 8711, and 8718 Å. The

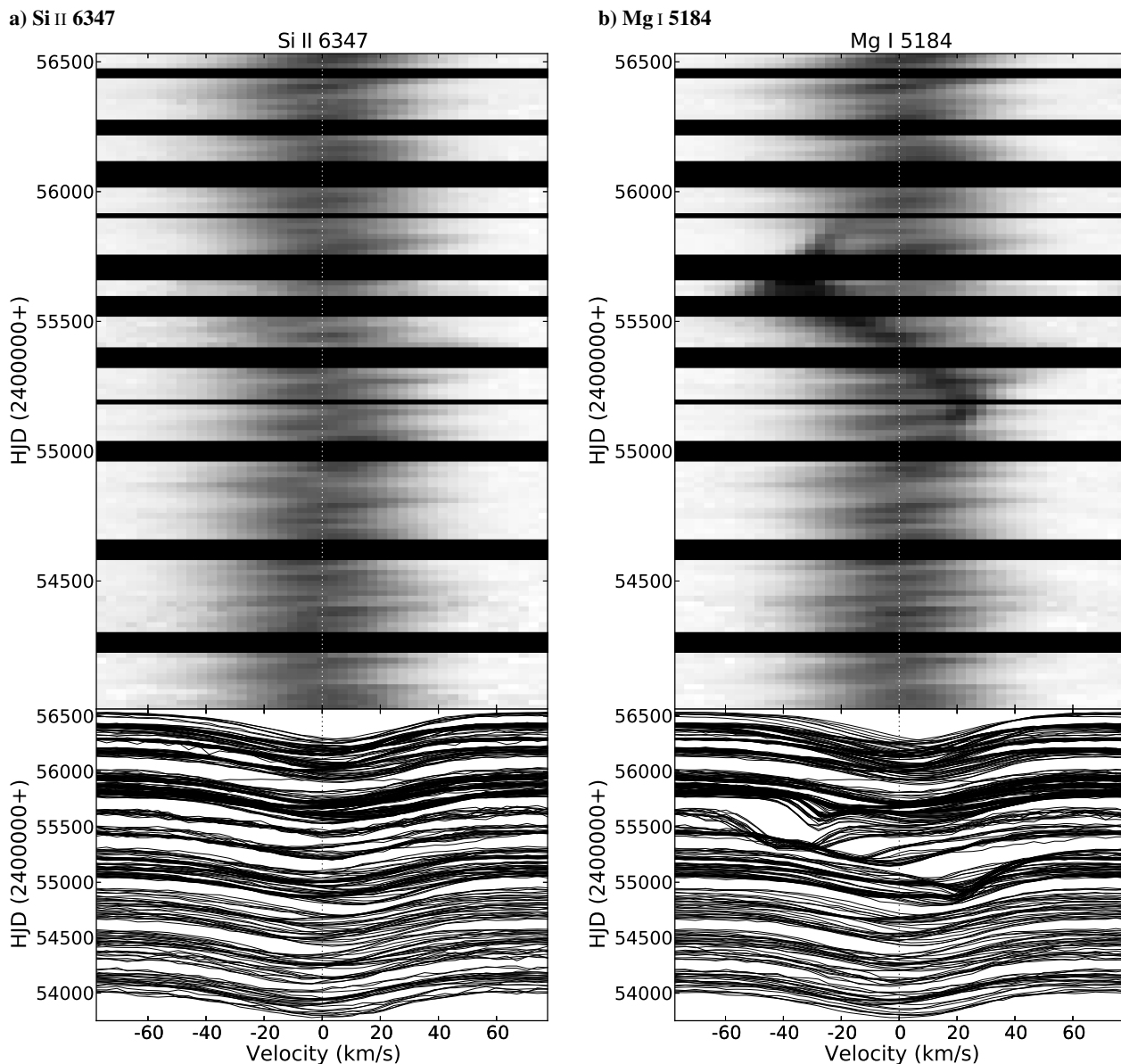


Fig. 3 Time series of optically-thin spectral lines. Panel **a** shows a representative example where no disk absorption appeared during eclipse (Si II 6347) while panel **b** shows a representative example where a disk absorption line appeared (Mg I 5184). A total of 207 lines in our spectra showed no disk imprint, a total of 161 lines did. Time increases from bottom to top. The orbital motion has been removed. Note that the gray scale in the upper panels represent minimum line depth (white) and maximum line depth (black).

N I 7468 line is representative of this group of photospheric lines. Irregularly spaced radial-velocity variations as well as line-profile changes are detectable in its dynamic plot. As for above Si II lines, we believe that these are due to the F0-star pulsation. The EW of the N I 7468 line was essentially constant at 340 ± 40 mÅ. The variations in radial velocity and equivalent width are not simply correlated. There was no significant influence of the eclipse to be seen in the equivalent width of this line nor were there any additional absorption features apparent.

3.4.3 H I Paschen lines

The Paschen series is detected in ϵ Aur from the strong Pa12 line at 875.0 nm down to Pa37 at 825.8 nm near the series end. However, lines with wavelengths shorter than 828 nm (Pa31) are so strongly contaminated by telluric lines that no profile detections are possible. Not even the more isolated Paschen lines show evidence for line profile variations due to the eclipse. The overall line strengths best fit those of the MK F0Ia standard star ϕ Cas. We also note that in a spectrum of the A9III MK-standard 32 Gem the lines weaken towards the series limit considerably faster than in ϵ Aur or ϕ Cas. While Pa12 is of comparable strength in all three stars with a residual intensity of 0.5, the Pa25 line is

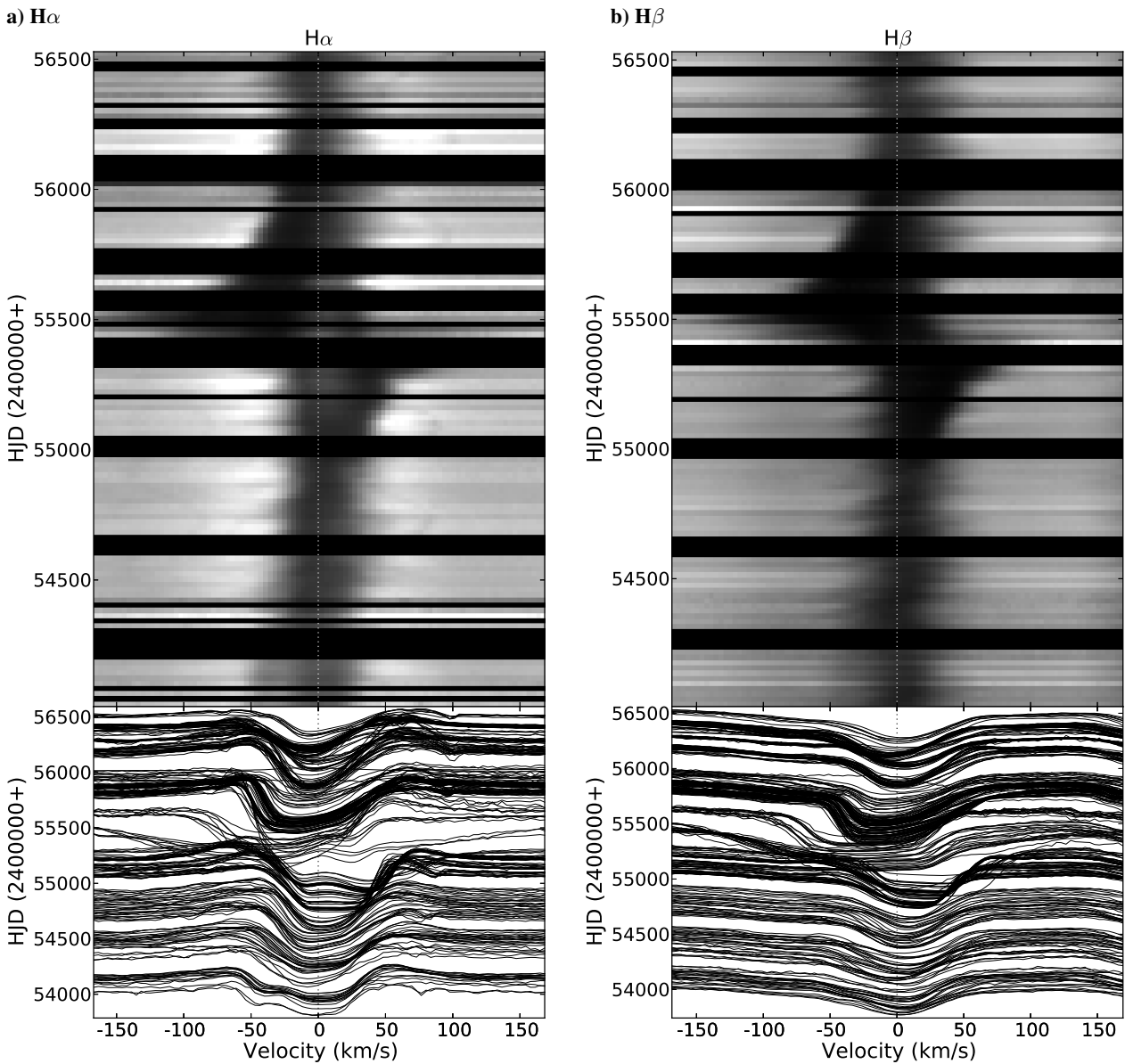


Fig. 4 Time series of hydrogen Balmer lines. **a** $H\alpha$, **b** $H\beta$. Note the doubling of $H\alpha$ during eclipse as well as the weak blue-shifted absorption at the beginning of our time series.

stronger in ϵ Aur and ϕ Cas by roughly a factor five. The line widths are in overall agreement when compared to ϕ Cas but broader than the higher-gravity star 32 Gem.

3.5 Spectral lines with disk absorption during eclipse

3.5.1 $H\text{I}$ Balmer lines

The Balmer absorption line profiles are significantly deformed during eclipse. Fig. 4a shows the line profile of $H\alpha$ over the entire observation period. Prior to eclipse a comparably sharp absorption component at -60 km s^{-1} was existent in the blue wing and moved towards line center even before the dust eclipse began. This component was also recorded by Chadima et al. (2011) where it was shown to appear suddenly around 2,453,500 (mid 2005). Schanne

(2007) and Chadima et al. (2011) had already noticed unusual $H\alpha$ variations as early as April 2005, much prior to the photometric dust-dominated eclipse. Then, the blue emission component of the profile had reversed into absorption and back to the regular emission. The latter must have happened in early 2006 and thus took almost a full year. A blue-shifted absorption component at around JD 2,453,500 far outside of eclipse is indeed surprising. Similar $H\alpha$ profiles were reported by Harrington & Kuhn (2009). This mysterious component is also seen in other strong lines, e.g. Na D, Fe II 4924, 5169 a.o.. Following up on Harrington & Kuhn (2009), Geise et al. (2012) showed that the $H\alpha$ -blue and red emission wings are not (linearly) polarized, indicating a symmetric emission source. They also found that the $H\alpha$ -

line core is not saturated, unlike $H\beta$, which means that extra emission is present, possibly even from the secondary star.

At the beginning of the eclipse, $H\alpha$ appeared like split into two absorption lines, where the already red-shifted component increased its red shift throughout ingress. During mid-eclipse near JD 2,455,300 this peak appeared at $+20 \text{ km s}^{-1}$ and then slowly decreased towards its rest wavelength within 300 days, disappearing completely near JD 2,455,600. After ingress a broad absorption component developed on the blue side of the line. Its absorption-wing edge reached -230 km s^{-1} of the rest wavelength for ≈ 50 days. During that time it coexisted with the fading red-shifted absorption mentioned above. Both components had basically vanished after egress. Unfortunately, we have a data gap starting exactly that time due to a technical CCD upgrade.

Our EW measures are shown in Fig. 5a. The overall equivalent width of $H\alpha$ does not change much during eclipse ingress (JD 2,455,070-270) but then rises rapidly, reaching a maximum EW at around JD 2,455,500. It then declines comparably rapid near JD 2,455,600 just to enter a more calmly declining phase until the end of the photometric eclipse at JD 2,455,800.

The behavior of the $H\beta$ profile (Fig. 4b) is in principle similar to that of $H\alpha$, and so are $H\gamma$ to $H\epsilon$ (not shown) of the Balmer series. Their equivalent-width development is accordingly similar. Fig. 5a compares the EW measures for $H\alpha$ and $H\beta$. At eclipse ingress $H\beta$ rises slower than $H\alpha$ but then shows a comparable sharp but more confined maximum at the same time as in $H\alpha$ (near JD 2,455,500). The declining phase after the maximum is also more gradual than for $H\alpha$ but equivalently does not end at 4th contact and continues beyond the end of our observations.

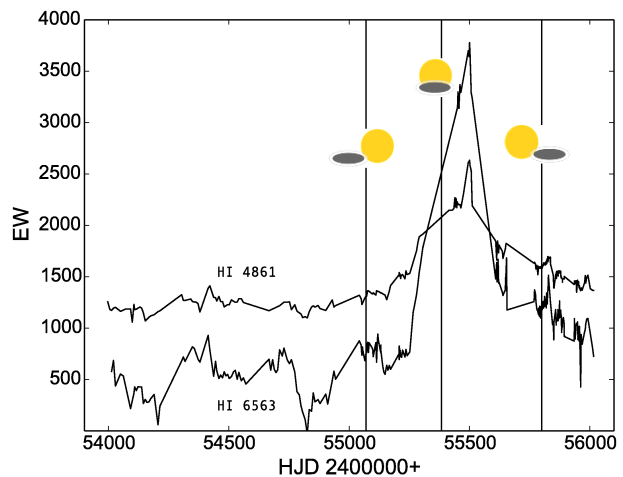
3.5.2 Mg I 5184

The Mg I 5184 absorption line shows a signature of the eclipse similar to that of the Balmer lines but without the overall double-peaked emission. The line's lower excitation potential is 2.71 eV, its upper potential 5.11 eV. During ingress a red-shifted absorption component rises for about 200 d, sweeps through the profile and then appears as a strong and complex-shaped blue-shifted absorption component. The detailed behavior of this line is very similar to that of the Ca I + Ti II 5189 blend. Fig. 3b shows the line-profile variation as a function of time. The equivalent width of the full line increases less dramatic during eclipse compared to the Balmer lines but decreases also sharply at egress (Fig. 5b).

3.5.3 Ca I + Ti II 5189

The transient absorption component in this line appears very comparable in strength and velocity to the feature in the Mg I 5184 line. The line's lower excitation potential is 1.58 eV, its upper potential 3.97 eV. The development of the

a) Balmer lines



b) Optically thin lines

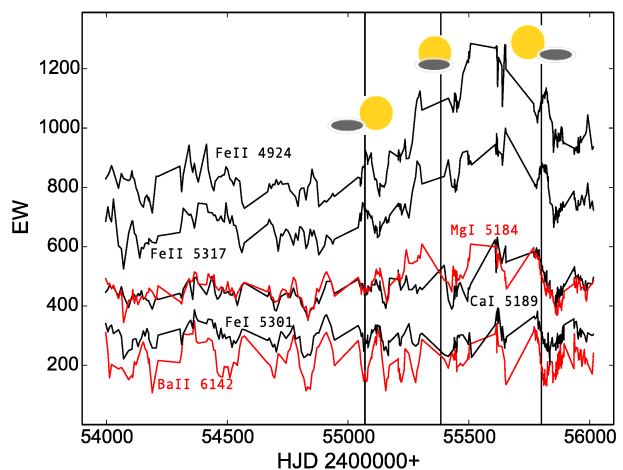


Fig. 5 Comparison of equivalent width changes. **a** $H\alpha$ and $H\beta$. **b** Representative lines from Sect. 3.4 and Sect. 3.5. Equivalent width is given in $\text{m}\text{\AA}$ and time is given in truncated Julian days.

equivalent width (Fig. 5b) also does not show any significant enhancement during the first half of the eclipse. But at 3rd contact (JD 2,455,630) the equivalent width had increased by around 30% and declined thereafter and beyond 4th contact.

3.5.4 Ba II 6142

The line is primarily assigned to Ba II (Lambert & Sawyer 1986) but the NIST Atomic Spectra Database² suggests also an iron blend (Fe I 6141.73) which is supported by the similar profile behavior of the Fe I-5031 line (see next subsection). The barium line's lower excitation potential is 0.70 eV, its upper potential 2.72 eV.

The line is remarkably variable in equivalent width before eclipse (Fig. 5b) which supports its Ba II origin because of its high temperature sensitivity. There is no significant

² <http://physics.nist.gov/PhysRefData/ASD>

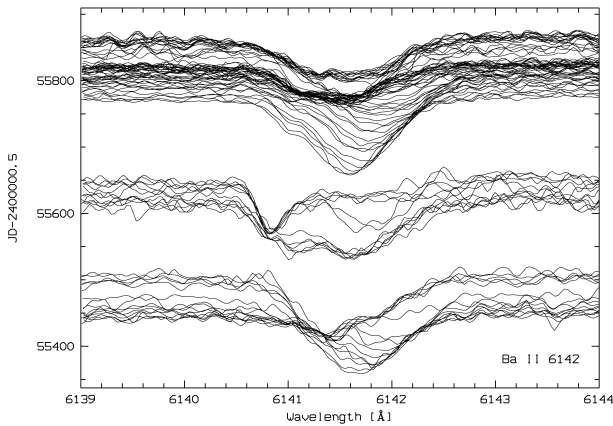


Fig. 6 Line-profile evolution of the Ba II 6141.7 line during eclipse. Shown are profiles between JD 2,455,440–870. Notice the almost complete disappearance of the regular photospheric absorption profile between JD 2,455,648–653 with only the narrow blue-shifted absorption line remaining.

change during the first half of the eclipse, but with 3rd contact at JD 2,455,636 a blue-shifted narrow absorption component appears at 6140.8 Å for a short time and then vanishes rapidly. The blue shift of the sharp disk absorption is -44 km s^{-1} relative to the rest wavelength of 6141.73 Å at 3rd contact. In four spectra between JD 2,455,648–653, the regular photospheric line almost completely disappears leaving just the blue-shifted transient absorption visible which again suggests its Ba II identification.

3.5.5 Fe I 5031

The behavior of this unblended Fe I 5030.78 line is very similar to that of the Ba II line. Its time series shows nearly identical absorption components despite that the line's lower and higher excitation potentials of 3.2 eV and 5.7 eV are very different to those of Ba II. The red-shifted absorption begins to develop at JD 2,455,600 and reaches its largest strength at JD 2,455,630. The blue shift is then about -36 km s^{-1} similar to but somewhat less shifted than in the Ba II line. The equivalent width of the line remains almost constant during the entire observing period (Fig. 5b), as did the Ba II - Fe I 6142 blend on average.

3.5.6 Fe II 4924

This line (4923.392 Å, low 2.9 eV, high 5.4 eV) is among the strongest of the optically thin lines and resembles the changes in H α , i.e. the appearance of a red shifted, very weak absorption component two months before ingress which then disappears after mid-eclipse. At that time it is substituted by a stronger and broader blue-shifted absorption component that decreases thereafter but persists beyond 4th contact (the end of the photometric eclipse). The line also shows the mysterious blue-shifted weak absorption component prior to first contact, similar to that in H α and H β , but reduced in strength. The evolution of the total line

equivalent width (Fig. 5b) shows an increase after 1st contact to up to 50% and reaches a maximum near mid-eclipse at JD 2,455,500 after which it declines. At 4th contact its value is still 250 mÅ larger than the pre-eclipse equivalent width of about 800 mÅ.

3.5.7 Fe II 5317 blend

This line is a close blend of two Fe II lines of comparable strength and excitation potential; 5316.610 Å, low 3.15 eV, high 5.5 eV and 5316.777 Å, low 3.2 eV, high 5.5 eV. It is not resolved in our spectra. The equivalent width of this blend does not increase significantly during the first 200 days of the eclipse (Fig. 5b) but it then rises sharply from 650 to 1000 mÅ until JD 2,455,300 and again declines during egress (JD 2,455,800). It does not show evidence of the pre-eclipse, blue-shifted, absorption component as in Fe II 4924, H α , a.o..

3.5.8 K I 7699 & 7664, Na I D_{1,2}, and other ISM DIB lines

The resonance doublet of neutral potassium K I (λ 7664, λ 7699) is located within the forest of lines from the terrestrial O₂ A-band at 7620 Å (Wallace et al. 1993). Their correct and coherent extraction over a long period of time is not without uncertainties and for the present analysis we decided not to remove the telluric spectrum. Fig. 7a shows the two K I lines over the period of our observations. The O₂ features in the two plots are the two A-band lines P(21,22) at 7664.9 Å and P(31,32) at 7698.9 Å, respectively. The photospheric K I absorption is not easily seen in the out-of-eclipse spectra of ϵ Aur (Fig. 7b) while the absorption from the disk dominates the eclipse spectra. The weak photospheric contribution matches the spectrum of the MK-standard ϕ Cas (F0Ia), which is of identical spectral type than ϵ Aur. However, the somewhat less luminous standard star α Lep (F0Ib) clearly shows both K I doublet lines (Fig. 7b).

The interstellar-medium (ISM) components in both K I lines (e.g. Chaffee & White 1982) are seen to persist throughout our observations. Both ISM features in ϵ Aur have similar line profile with a stronger blue-shifted absorption dip near the photospheric rest wavelength (average EW for λ 7699 of 85 mÅ) and a weaker red-shifted absorption dip (EW for λ 7699 of 35 mÅ). A comparison of this ISM feature with other supergiants at farther and closer distances than ϵ Aur, but vastly different positions in the sky, is shown in Fig. 7b. The distances listed are the nominal *Hipparcos* distances from van Leeuwen (2007) which sometimes are extremely uncertain, just like for ϵ Aur. The blueshifted-to-redshifted ratio is mostly different than for ϵ Aur except, maybe, HD 10494 at 6250 pc which has, however, overall stronger ISM absorption. It also has a much stronger photospheric K I line though, other than ϵ Aur, and appears just like in the nearby F5Ib star α Per which, on the other hand, is free of ISM lines. The in-of-eclipse spectrum of ϵ Aur in Fig. 7b qualitatively best resembles that of HR 825

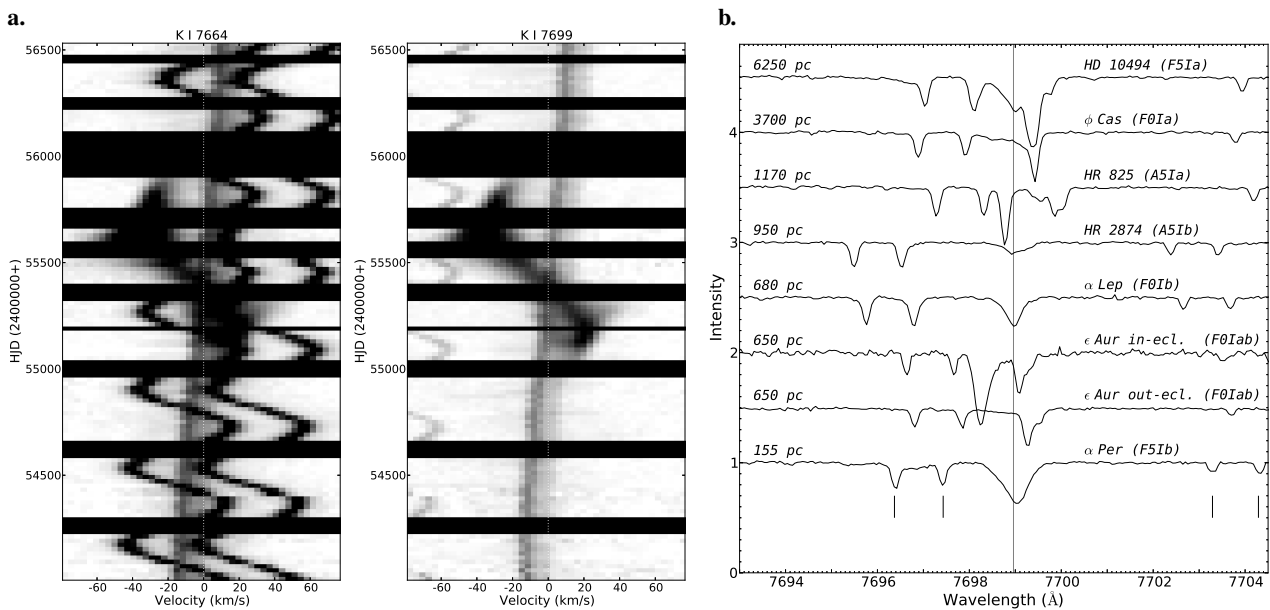


Fig. 7 **a.** STELLA time series of the resonance doublet K I 7664 (left) and K I 7699 (right). The disk transit is partly masked by telluric lines but clearly seen in both K I lines. Only a very weak photospheric contribution from ϵ Aur is seen. Notice the stationary interstellar components (appear slanted over time in the gray-scale plots due to the removal of the binary motion of ϵ Aur). Both wavelength regions are contaminated by telluric O₂ lines, in particular 7664 Å (these lines appear with a sinusoidal velocity variation due to the barycentric correction). **b.** A comparison of the K I 7699-line region with other supergiants at increasing distances from bottom to top. The nominal *Hipparcos* distance is indicated on the left, the MK-class on the right. The vertical line is the rest wavelength of K I 7699. The ISM lines are the sharp lines around this wavelength, mostly on the red side. The marked weak lines are of telluric O₂ origin.

(=V480 Per) at $d=1170$ pc. The latter's strongest line in the wavelength region shown is either from the companion star of this binary system or even is due to disk absorption just like in ϵ Aur. While ϕ Cas at 3700 pc best matches the line strength of the blue-shifted ISM feature in ϵ Aur, it exhibits no red-shifted absorption component at all.

Both sodium lines of ϵ Aur are dominated by circumstellar- and interstellar absorption. Fig. 8 shows time series and profiles for the D₁ and the D₂ lines. Both lines trace the eclipse just like H α and H β rather than K I or other optically-thin lines which suggests a significant or even dominating disk-halo contribution during eclipse. It is particularly noteworthy that a blue-shifted Na I absorption is already present at the onset of our observations three years prior to the eclipse. Fig. 8 shows it gradually moving towards the orbital motion of the F-supergiant with a differential velocity of $52 \text{ m s}^{-1}/\text{d}$, significantly larger than the differential orbital motion of the two stellar components, and disappeared one year before ingress at JD 2,454,500. The feature reappears immediately after egress with increased strength but with a stationary location in the time-velocity plane. This feature is likely associated with a halo around the accretion disk and apparently moves along the orbital path of the secondary star.

Diffuse interstellar bands (DIB) were also measured in the spectra of ϵ Aur, i.e., DIB $\lambda 6613$ (EW=128 mÅ), $\lambda 8621$ & $\lambda 8650$ (not detected), $\lambda 5780$ (285 mÅ), and $\lambda 5797$ (77 mÅ). The $\lambda 8621$ & $\lambda 8650$ bands are not detected in any of the stars in Fig. 7b and maybe due to the relatively strong,

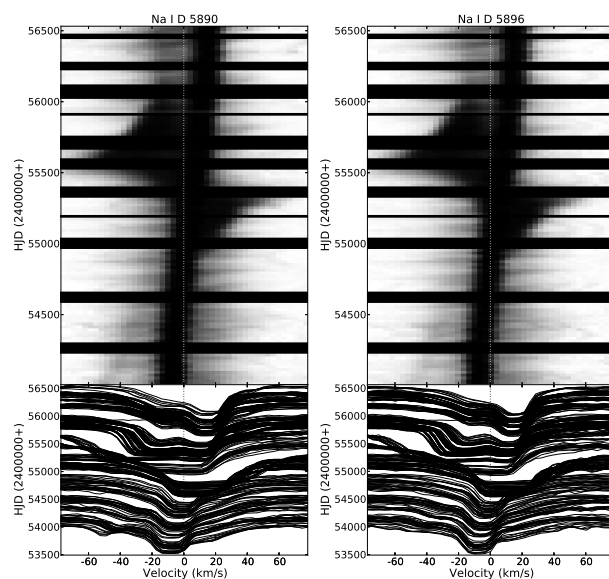


Fig. 8 Time series of the resonance doublet Na I 5890 (left) and Na I 5896 (right). The disk transit is partly masked by the stationary interstellar components that, like in K I, appear slanted over time due to the removal of the binary motion of ϵ Aur. Only a weak photospheric Na I D contribution from ϵ Aur is seen which shows the same pulsation pattern as is displayed in, e.g., Fig. 3. Note the migrating blue-shifted absorption before the start of the eclipse, just like in H α , H β and some Fe II lines, and the remaining extra absorption after eclipse.

close-by Si I 8650.8-Å line in supergiants. For DIB λ 6613, we measure total EWs between 40 mÅ (α Lep, $d=680$ pc) and 295 mÅ (HD 10494; $d=6$ kpc). We note that our EW λ 6613 for HR 825 = HD 17378 of 303 mÅ is rather different to the 430 mÅ measured by Wallerstein et al. (2007) with comparable spectral resolution, while its values for, e.g., λ 5780 precisely agree to within a few per cent. The line is likely affected by the local environment around HR 825.

While our supergiant standards show a general tendency of increased EW with distance – independent of the position in the sky – it is not possible to conclusively relate the DIB strength in ϵ Aur to its distance. However, a distance greater or equal than ≈ 1 kpc and less than 3.7 kpc is favored.

4 F-star rotation

4.1 The problem

Determining the stellar rotational velocity in the presence of surface pulsation of comparable amount is uncertain on its own but doing so for an F0 supergiant with expectable non-LTE and spherical effects is a non-trivial task and appropriate non-LTE computations are beyond the scope of this paper. Not surprisingly, $v \sin i$ values for ϵ Aur in the literature vary between 5 to 50 km s⁻¹. A more recent value is the 38 km s⁻¹ from a Fourier decomposition of the nitrogen triplet from $R=45,000$ spectra by Potravnov (2012). Sadakane et al. (2010) quoted a combined rotation and macroturbulence broadening of ≈ 27 km s⁻¹ from their $R=65,000$ spectra while Griffin & Stencel (2013) applied a rotational velocity of ≈ 36 km s⁻¹ to fit their spectra but quoted no macroturbulence. Lucy (1976) first confirmed that the macroturbulent line broadening of hot supergiants becomes essentially identical to the expected pulsation line broadening due to their atmospheric pulsation pattern. Aerts et al. (2009) concluded that the physical explanation for macroturbulence in hot massive stars is basically gravity modes with degrees less than 10. They presented line-profile simulations that showed that $v \sin i$ can be seriously underestimated in such cases and even concluded that better $v \sin i$ results are obtained if the classical macroturbulent broadening is not included simultaneously in the line-profile fitting process.

4.2 Spectrum synthesis

Our PARSES value (see Sect. 3.2 and Table 3) for $v \sin i$ is 28 ± 3 (rms) km s⁻¹ and is based on a least-squares comparison of the $R=55,000$ STELLA spectra with synthetic LTE models from plane-parallel model atmospheres. This value is a grand average from 474 individual spectra, each already an average from approximately 300 individual spectral lines. Although the grand rms deviation is just 3.0 km s⁻¹ the rms from the line average of an individual spectrum can be significantly larger with up to ± 10 km s⁻¹ depending on the S/N ratio of the spectrum. The strength of this approach

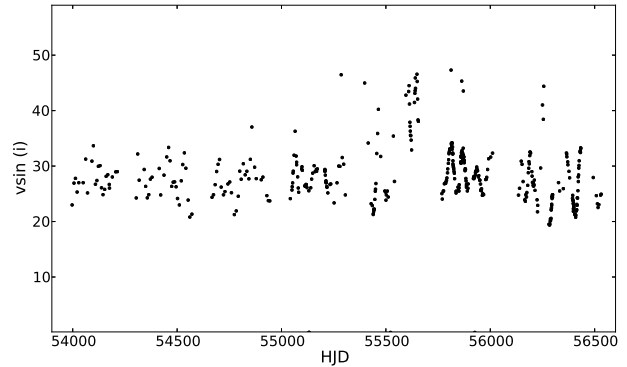


Fig. 9 Time series of the average residual line broadening $v \sin i$ in km s⁻¹. Note that the velocity v is a combination of rotation and pulsation. We interpret the long-term average of 28 ± 3 (rms) km s⁻¹ to be due to rotation and the temporal variations of up to 15 km s⁻¹ peak-to-valley to be due to pulsations. The best-fit period for the variations at and after egress is 62.6 ± 0.7 d. No single clear period is found for ingress and before.

is that we solve for $v \sin i$ simultaneous with microturbulence while keeping the macroturbulence fixed. However, we implicitly neglect the extra line broadening due to inhomogeneous non-radial pulsation effects beyond macroturbulence.

4.3 Comparison with other supergiants

For a double check, we verify $v \sin i$ via a simple comparison with slowly-rotating standard stars of known $v \sin i$ and comparable MK classification. This approach is largely independent of the actual values for the micro- and macroturbulence because we can assume that they are identical, or nearly so, for identical MK classification. The FWHM then directly relates to $v \sin i$. Fig. 1 compares a spectrum of ϵ Aur with two such standards; α Lep (F0Ib) and ϕ Cas (F0Ia). While α Lep has fairly sharp lines, ϕ Cas has considerably broader lines but not quite as broad as ϵ Aur. Previous $v \sin i$ determinations of α Lep span the range from 21 km s⁻¹ (Royer et al. 2002) to 13 km s⁻¹ (Abt & Morrell 1995), both taken at similar spectral resolution of $\approx 16,000$ at KPNO and OHP, respectively. For ϕ Cas, the same sources give 31 km s⁻¹ and 23 km s⁻¹, respectively. Our PARSES values for three S/N \approx 350:1 STELLA spectra of α Lep are 7.6 ± 1.5 km s⁻¹, 9.2 ± 1.5 km s⁻¹ and 8.1 ± 1.5 km s⁻¹ and thus drastically smaller than the literature values. Three equally well exposed spectra of ϕ Cas gave 24 ± 2.5 , 25 ± 3 , and 20 ± 3 km s⁻¹, in good agreement with Abt & Morrell (1995). The average FWHM from weak lines is 0.94 Å (ϵ Aur), 0.28 Å (α Lep), and 0.78 Å (ϕ Cas) in excellent agreement with our PARSES $v \sin i$ values. This assures the confidence in our spectrum synthesis result above.

5 Line-profile variability

Examples of the line-profile variability inside and outside of eclipse are shown in Figs. 3, 4 and Fig. 6. Line-profile variability is clearly visible in all spectral lines, even in those that are not obviously affected by the eclipse. Characteristic absorption bumps are moving across the line profile from blue to red on a time scale of ≈ 60 d. These bumps were already noticed in previous papers by e.g. Chadima et al. (2011) and Harmanec et al. (2013). Only the Balmer $H\alpha$ line exhibits additional emission in the wings.

5.1 F-star oscillations

5.1.1 From line broadening

We first analyze the observed average line broadening as it represents a global surface proxy for the combined oscillation and rotation pattern. Our spectral time series consists of the 474 spectra between 2006 and 2013. As introduced in Sect. 3.2, we fit a large wavelength range of each observed spectrum with a synthetic spectrum. Microturbulence and macroturbulence were set to 10 km s^{-1} each and kept fixed during the fits. The remaining average line broadening is then attributed to a combination of stellar rotation and non-radial pulsation. Because stellar rotation must not vary during our observational period, even if it had a complicated differential-rotation pattern, we attribute the long-term average line broadening to rotation and the varying part to non-radial pulsation. Its long-term average and rms over the almost 7 years of data was 28 km s^{-1} and just 3 km s^{-1} , respectively, even including the eclipse phases. This is exactly the same value that we got from the independent analysis in Sect. 4.

However, these residuals appear to vary systematically with time, in particular during and after eclipse egress but less so outside of eclipse and during ingress. Fig. 9 shows the line-averaged broadening expressed as $v \sin i$ as a function of time for the entire STELLA observing period. A Lomb-Scargle periodogram of the line-broadening residuals from 2011-2013 shows a clear peak at 62.6 ± 0.7 d with a full amplitude of $9 \pm 2 \text{ km s}^{-1}$ (a second but weaker period is apparent at 56.7 d). No such clear period(s) are found for the years prior to mid eclipse from 2006-2010, although variations of similar amplitude are seen, but obviously without phase coherence. The variation is most obvious in the 2011/12 observing season and even shows amplitude evolution as expected for multi-periodic non-radial patterns.

5.1.2 From line-profile bumps

Our next step is to employ the information from the line profiles. We recall that Fig. 3 compares the dynamical spectral-line profiles of the Si II-6347 and the Mg I-5184 lines. While the latter line is heavily distorted during eclipse with an extra absorption dip from the disk sweeping through the profile from the red wing to the blue and back, the former line

is among the 207 eclipse-insensitive lines. However, both line groups show the same short-term profile variability that is likely due to excited surface-oscillation modes. The figure also demonstrates that the F-star oscillations continue to modulate the disk-affected spectral lines throughout the eclipse and are thus physically not related with the disk.

Two-dimensional periodograms are built by applying a simple Fourier analysis to each wavelength pixel within a spectral line profile as a function of time. We use the program package MuFrAn (Multiple Frequency Analysis; Kolláth 1990). The “bandwidth” is thereby defined by the pixel dispersion of the detector at the wavelength used. Note that the echelle data reduction does not re-sample the entire spectrum to a constant dispersion but that the dispersion varies between 0.0246 \AA/pix for the mid point of the bluest echelle order to 0.0549 \AA/pix for the mid of the reddest echelle order. Fig. 10 shows the results. Panels Fig. 10a-d show the 2D periodograms for Si II, Mg I, $H\alpha$ and $H\beta$, and reveal a rich structure of frequencies with the dominating frequency at a period of 110 ± 3 d, best seen in the red wing of each spectral line. A weaker peak with a frequency of 0.135 c/d ($P=74 \pm 3$ d) consistently appears in all line profiles. We note that the line cores are remarkably free of frequencies. This would be qualitatively in agreement with numerical simulations that show that rapid rotation focuses low degree modes towards the equator and thereby lead to increased variability in the line wings (Reese & MacGregor 2013). The disk-free spectral lines consistently show three groups of frequencies centered at average periods of approximately 40 d, 60 d, and 110 d.

5.1.3 From line-depth-weighted radial velocities

A line-depth weighted central wavelength was computed for each line profile by building the ratio of the weighted to the unweighted intensity summed over all pixels within a profile. This “center of intensity” is a 1-d representation of the line-profile distortion. The respective top panels in Fig. 11 plot the time series of these central wavelengths expressed as radial velocities for the four example lines Si II 6347, Mg I 5184, $H\alpha$ and $H\beta$. Although there are clear and coherent variations with amplitudes of up to 10 km s^{-1} , neither a stationary Lomb-Scargle nor a stationary FFT periodogram showed a single strong period. Therefore, we employed an adapted version of the program package TiFrAn (Time Frequency Analysis; Kolláth & Oláh 2009) for non-stationary time series. Its results are shown in the respective lower panels in Fig. 11. Now, two dominant periods become evident for the time before the eclipse (on average 118 d and 153 d). Towards the end of our data set, and certainly after mid eclipse, these two periods seem to have drifted to longer values of 127 and 172 d with errors of up to $\pm 6-7$ d for any of them, respectively. A third, significantly shorter period of ≈ 90 d appeared after mid eclipse and is seen in all four line tracers in Fig. 11. Note that the time coverage is ≈ 2500 d with nearly continuous sampling. If real, it would indicate a positive drift rate opposite to what was recently found for

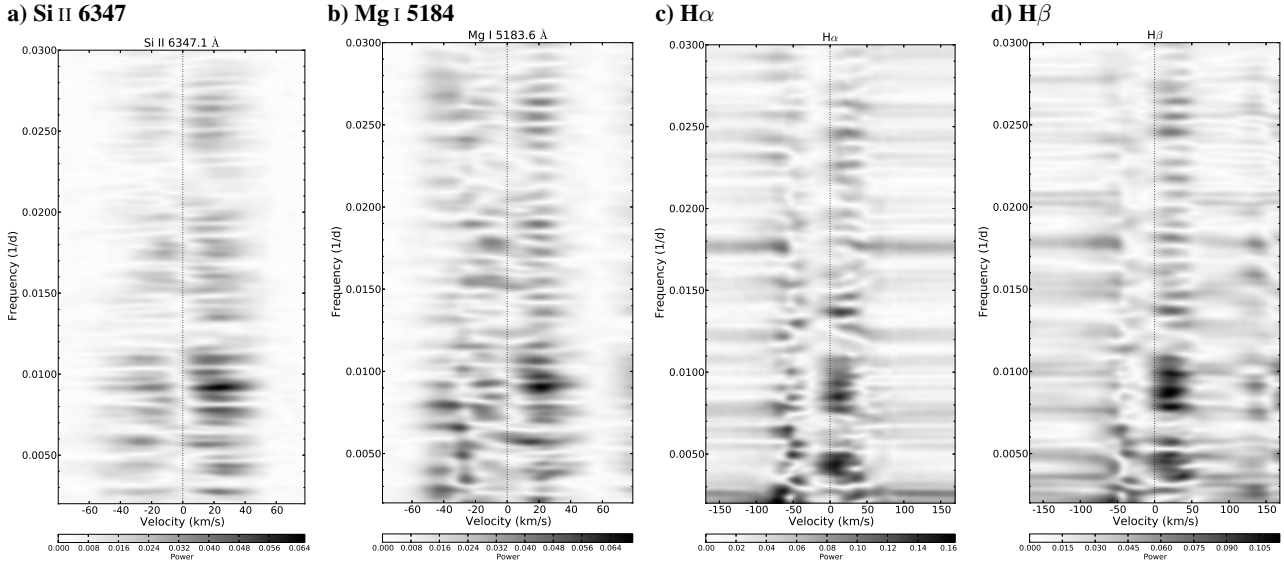


Fig. 10 Two-dimensional periodograms for the four spectral lines already shown in Fig. 3 and 4. Plotted is spectral power as a gray scale in a frequency versus velocity domain centered at the respective rest wavelength. Note the larger velocity plot range for the Balmer lines. The frequency range equals a period range between 400 d (bottom) to 33 d (top).

the two dominating periods from inter-eclipse photometry by Kloppenborg et al. (2012) (see Sect. 6 for more details).

It is worthy to note that the CHARA images (see insert Fig. 2) show that the obscuration by the disk is slightly off the equatorial plane of the supergiant which means that at first contact the disk is not blocking the stellar equator but only some higher latitudes. This requires that the disk absorption could only set in at projected stellar radial velocities lower than $v \sin i$ of the supergiant ($+28 \pm 3 \text{ km s}^{-1}$ see Sect. 4). Given the total line width of approximately $\pm 60 \text{ km s}^{-1}$, such a low (red) shift would be possible only if the pulsation pattern has a multi-mode non-radial structure with sectoral nodes of low order, say, $\ell, m \approx 2 - 3$ and its main velocity variation time scale is long compared to the variation time scale due to the disk transit. Also note that the very first disk absorption spectra at around 2,455,100 do not disrupt or in any way dim the background stellar line profiles suggesting that the pulsation-velocity pattern is symmetric in azimuthal direction. The fact that the line-profile variability remains qualitatively the same within the eclipse additionally suggests that either the one un-eclipsed rotation pole of the F star carries all the pulsation information or, equally likely, that the number of sectoral and tesseral modes is high enough so that the obscuration due to the disk has no effect on the period detection.

5.2 F-star wind and upper atmosphere

The $H\alpha$ line shows a double-peaked asymmetric emission profile with variations extending to about $+100 \text{ km s}^{-1}$ and -150 km s^{-1} from the line center, thus significantly beyond the $v \sin i$ of 28 km s^{-1} . This indicates a stellar wind from the F supergiant. Qualitatively, the profiles resemble those of mass-outflow red giants, e.g. like the ones in low-

Table 4 Results from the spectroscopic period analyses.

Tracer	Period (d)	Note
<u>Optically thin lines:</u>		
Residual line broadening	62.6 ± 0.7	after mid eclipse
Line-profile bumps	≈ 38	line wings
	≈ 64	line wings
	74 ± 3	red wing
	110 ± 3	line wings
Line-depth-weighted RVs	118 ± 6	before mid eclipse
	153 ± 5	before mid eclipse
	90 ± 5	after mid eclipse
	127 ± 6	after mid eclipse
	172 ± 7	after mid eclipse
<u>Balmer lines:</u>		
Line-profile bumps	56.8 ± 0.7	for $v > v \sin i$
	73 ± 2	for $v \leq v \sin i$
	116 ± 6	for $v \leq v \sin i$
	224 ± 8	(alias?)
Line-depth-weighted RVs	110 ± 6	before mid eclipse
	140 ± 5	before mid eclipse
	83 ± 5	after mid eclipse
	130 ± 7	after mid ecl. $H\beta$
	165 ± 10	after mid eclipse

metallicity globular clusters (Meszaros et al. 2009). Note though that most of the line-profile variability in $H\alpha$ and $H\beta$ resides within the red-shifted emission wing at $+50 \text{ km s}^{-1}$ from the line center. The same morphology is also evident in $H\gamma$ and $H\delta$.

Fig. 10c shows the two-dimensional periodogram from $H\alpha$. It generally reveals longer periods for radial velocities smaller than $v_{\text{rot}} \sin i$, i.e. closer to the line core, as compared to velocities larger than this. The most dominant pe-

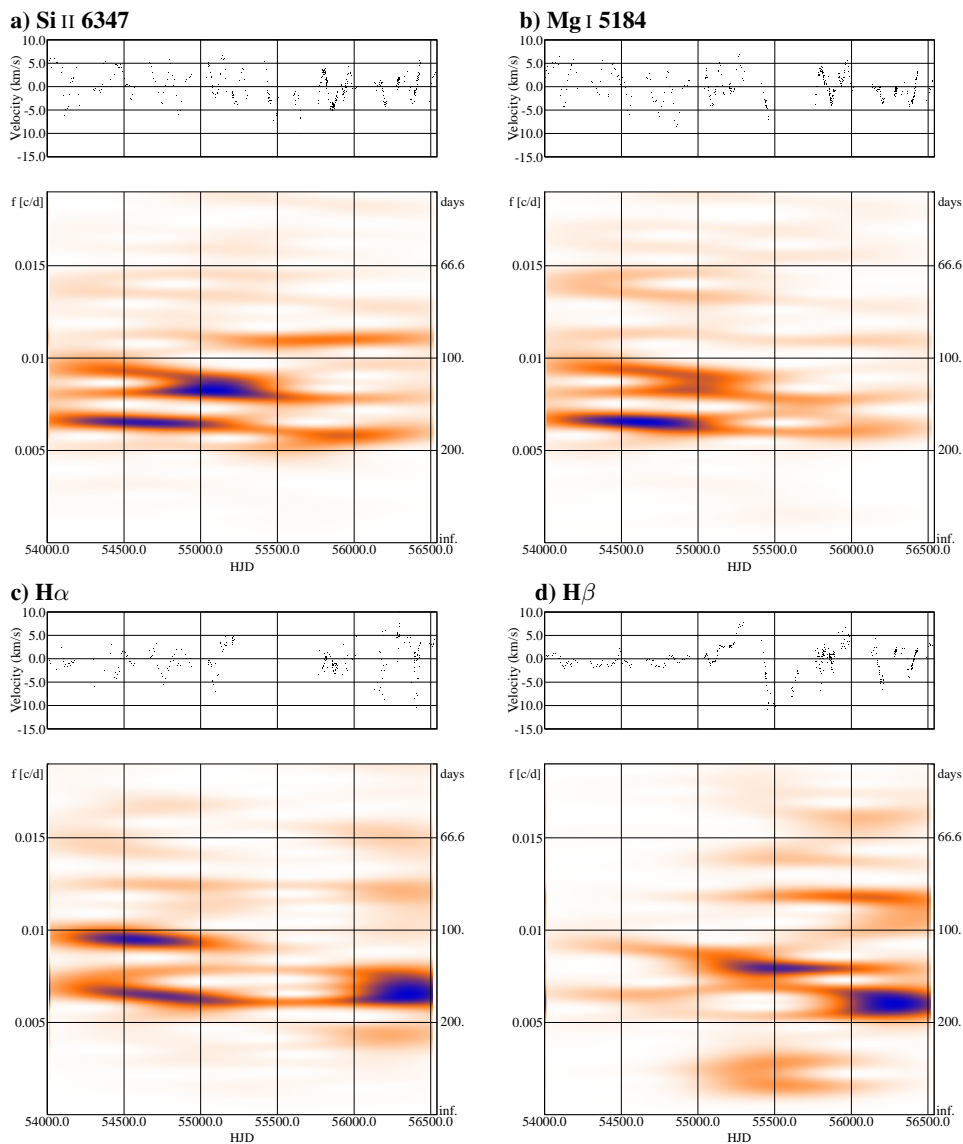


Fig. 11 Radial velocity variations from the line-depth weighted central wavelengths (respective top panels) and their periodograms from short-term Fourier transforms (respective lower panels). Shown are the results for the four example lines **a** Si II 6347, **b** Mg I 5184, **c** H α and **d** H β . Notice the existence of two dominating, time-dependent, periods from around 120 d and 150 d in 2006/7 (JD 2,454,000) to 130 d and 170 d in 2012/13 (JD 2,456,500), respectively.

riod for pixels with $v > v_{\text{rot}} \sin i$ is $\approx 56.8 \pm 0.7$ d while for $v \leq v_{\text{rot}} \sin i$ we see three almost equally strong groups of periods at $\approx 73 \pm 2$ d, 116 ± 6 d and $\approx 224 \pm 8$ d. One of the latter two appears to be the alias of the other. The 116-d period could be the same as the 110 ± 3 -d period from the optically-thin lines. For comparison, the H β line is dominated by a period of 115 ± 10 d, again in agreement with the period from H α and the photospheric optically-thin lines. The other two periods seen from H α are also present in H β but comparably weaker with nominal values of 72.5 ± 2 and 222 ± 12 d. Outside of the rotationally broadened line profile (i.e. ± 50 – 150 km s $^{-1}$), H β shows a dominant period at 56.0 ± 0.8 d in good agreement with the 56.8-d period from H α (evidently mostly in the blue line wing). It also coincides with the “second” period from the average line broad-

ening in Sect. 5.1.1. This could be just apparent though and due to the complex non-radial surface pattern. Table 4 summarizes the period results. A 56-d period is close to the 62.6-d period seen from the line width variation of optically-thin lines in 2011–13. However, the error bar on each of them is less than 1 d and thus the two periods formally do not agree. It is tempting to speculate though that the shorter period from the H α and H β (and H δ) wings arises from layers further up in the atmosphere but have otherwise the same pulsation origin.

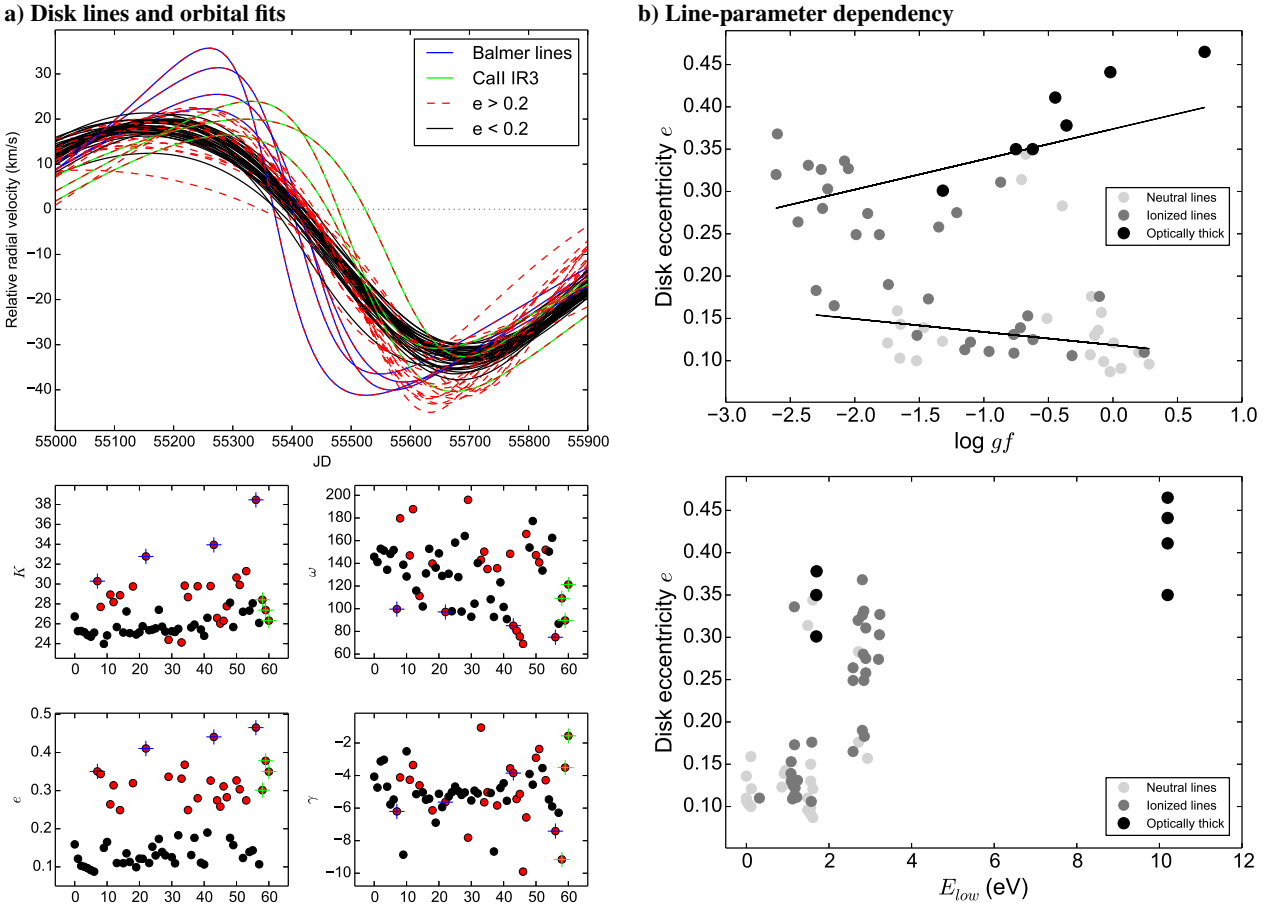


Fig. 12 Disk rotation profiles. **a** The top panel plots the disk-absorption radial velocities relative to the supergiant. Shown are 61 spectral lines versus time. Time is in fractional JD24+. The lower panels show the disk orbital-fit parameters as a function of spectral line (integer numbers); K , half amplitude in km s^{-1} , e disk eccentricity, ω longitude of the disk periastron in degrees, γ disk center-of-mass velocity in km s^{-1} . The blue crossed circles denote the first four Balmer lines, the red crossed circles the Ca II IRT lines. **b** Line parameter dependencies. The top and bottom panels plot e versus the logarithmic transition probability ($\log gf$) and the lower excitation potential E_{low} in eV, respectively. Parameterized are neutral and singly-ionized optically-thin lines as well as the three IRT lines and the four Balmer lines.

5.3 Disk rotation

5.3.1 The disk dimensions

Interferometric data suggest a disk “length”³ of 7.31 ± 0.66 au if at a distance of 737 ± 67 pc or ≈ 8.9 au if at 1 kpc (c/o Stencel 2012, 2013). It refers to the optically thickest portions and thus to a minimum disk size. The K I-lines suggest a disk length of more like 10 au. The disk thickness was given to 0.6 au and the separation of the two stellar components to ≈ 25 au, again courtesy of the review papers by Stencel (2012, 2013).

5.3.2 The disk rotation profile

The disk rotation is seen as a sinusoidal radial-velocity variation of its sharp absorption lines around the orbital velocity of the (unseen) secondary star, e.g. from Mg I 5184 Å in

³ ... or “diameter” if the disk were symmetric around its center of mass.

Fig. 3b. This sinusoidal variation is evident in our spectra in a total of 161 spectral lines of a variety of atomic properties. While the overall variation is due to the presumably Keplerian rotation of the disk, subtle differences from line to line may reflect the radial physical conditions within the disk.

Saito et al. (1987), Lambert & Sawyer (1986) and Ferluga & Mangiacapra (1991), a.o., had examined the disk-rotation profile for previous eclipses. It was found that all eclipses monitored so far showed the same unequal radial-velocity amplitudes between ingress and egress with absolute values of around $+20 \text{ km s}^{-1}$ at ingress and -40 km s^{-1} at egress, a fact already noted by Struve et al. (1958). If the disk rotation indeed obeys a Keplerian velocity distribution, this difference of $\approx 20 \text{ km s}^{-1}$ suggests that the disk is highly elliptical with the secondary star closer to the edge of the disk at egress. The average maximum red shift of the disk lines in 2009-11, e.g. from Mg I, is $20.8 \pm 0.8 \text{ km s}^{-1}$, the average maximum blue shift is $-36 \pm 2 \text{ km s}^{-1}$, comparable to the values already found during the 1982-85, 1955-57,

and possibly the 1928-30 eclipses (see Lambert & Sawyer 1986). Thus, the accretion disk “contacts” the projected supergiant disk at a radial velocity of $+20.8 \text{ km s}^{-1}$ which equals the projected stellar rotational velocity near a stellar latitude of $\approx 40^\circ$ (from our equatorial $v \sin i$ of 28 km s^{-1}), in good agreement with the CHARA image in the insert of Fig. 2. It also implies that the rotation axis of the F supergiant is perpendicular, or nearly so, to the orbital plane.

From our example line Mg I 5183.6 Å, the time between first appearance of the initially red-shifted disk lines and when they cross at zero relative velocity, i.e. when they appear at their respective rest wavelengths after correction of the binary motion, is $367 \pm 3 \text{ d}$. The time between zero relative velocity and disappearance of the then blue-shifted lines is significantly longer, $487 \pm 3 \text{ d}$. The time from maximum red shift to zero relative velocity is $270 \pm 5 \text{ d}$, and from zero relative velocity to maximum blue shift is $267 \pm 5 \text{ d}$, the latter two equal to within its measurement errors. Note that its zero relative radial velocity occurred at JD 2,455,413 \pm 4. The different ingress/egress durations with respect to this zero velocity are consistent with an elliptical disk in the direction of its orbital motion around the supergiant. The disk side with the higher-velocity amplitude spent more time in eclipse than the one with the lower-velocity parts. This would be at odd with a pure Keplerian disk motion but explainable if there is an extra velocity component from a mass stream from the supergiant (Griffin & Stencel 2013).

We try to quantify the disk rotation by directly measure the radial velocities of the transient absorption for all spectral lines. It is measured relative to the spectral lines of the F-supergiant primary. Out of the total of our 161 spectral lines that show such a transient feature, 61 appeared unblended enough for a reliable reconstruction. We note that all line profiles are affected by the migrating supergiant pulsation pattern. It imprints an additional variable absorption component of sometimes comparable strength than the transient disk absorption itself. Moreover, the amplitude of the pulsation pattern is different from line to line and can not easily be reconstructed e.g. from the lines that are not affected by the transient disk and then subtracted. Even for the 61 least-blended lines, we first had to fit a simple sine curve to the 2d-dynamic spectra in order to roughly identify the expected radial velocity range of the transient feature. Disk radial velocities were then measured by finding the minimum residual line intensity in a range $\pm 10 \text{ km s}^{-1}$ within this expected radial velocity. This prevents us from false O–C minima and at least minimizes the impact of the background pulsation pattern. In a next step, we treat the 61 disk radial-velocity curves just like binary-star radial-velocity curves and fit a fake binary orbit to every one. The orbital K -amplitude then represents the average rotational velocity of the disk. Our initial fits left all disk-orbital parameters free, although some are tightly constrained, e.g., the “orbital period” P by the duration of the transit, or the time of conjunction T_0 by the time when the relative radial velocity is zero. The “systemic disk velocity” (γ) is ex-

pected to be near the orbital velocity of the secondary star according to the binary orbit from Stefanik et al. (2010). After an initial parameter study, we kept the required “orbital period” fixed to an average value of 1,192 d (3.3 yrs). Saito et al. (1987) obtained a maximum disk rotational velocity of $42 \pm 2 \text{ km s}^{-1}$ and concluded on an orbital period of the disk of $\approx 3 \text{ yr}$.

Fig. 12a shows the resulting disk-rotation profiles from 61 absorption lines together with their fit parameters. All individual spectral-line data and traces can be found in the appendix in Fig. C1. The transients cluster into two families. Firstly, the majority can be fitted with low orbital eccentricity, $e < 0.2$ (on average 0.12), and low amplitude, $K \approx 26 \text{ km s}^{-1}$. Secondly, about one third of the lines show high-eccentricity fits, $e=0.25\text{--}0.45$, with generally also higher velocity amplitudes, $K \approx 28\text{--}38 \text{ km s}^{-1}$. The line with the highest eccentricity and amplitude is H α ($e = 0.46$ and $K = 38 \text{ km s}^{-1}$), almost matched by the other Balmer lines (H β , H γ , and H δ) and the three Ca II infrared triplet lines. The high-velocity transient absorption in these Fraunhofer lines is expected to originate mostly from the disk halo rather than the (dusty) disk in general, which then would indicate that the halo is even more asymmetric in shape than the disk itself. It is further evidence that the ϵ -Aur disk is a CV-like accretion disk with a mass stream from the F-supergiant and consecutive accretion onto the hidden secondary rather than just a proto-planetary optically-thick disk. Such a double-component picture, inner dusty disk plus a gaseous halo, agrees with the model by Budaj (2011) who proposed an inner optically-thick disk coated by an outer optically-thin disk to explain the mid-eclipse brightenings. Moreover, the higher velocity amplitudes of the Fraunhofer lines may indicate an additional non-rotational component, e.g. due to a shock front in the direction of the orbital motion or an asymmetric disk wind or a flaring inner disk.

Another detail in Fig. 12a is that the transient absorption in H α crosses the relative zero-velocity line 45 days earlier than the majority of the optically-thin lines, while the Ca II infrared triplet lines cross it on average 80 days later. In general, all high-eccentricity spectral lines show a later crossing compared to the low-eccentricity lines. One exception in Fig. 12a appears to be Ti II 4464 Å. Close inspection of its profile shows it to be an unresolvable blend with Mn I and Fe I though, and thus may represent a bad measurement. Nevertheless, the different timings indicate an asymmetry of the transiting body and can be interpreted in different ways, all of them somewhat speculative. Firstly, one could imagine a binary system as the (unseen) secondary star where one component is responsible for the bulk of Balmer absorption, i.e. a hot and massive star, while the other component is responsible for the Ca II infrared resonance absorption, i.e. a late-type less-massive star. This is unlikely though because also strong singly-ionized lines with high excitation potentials show the late crossing, such lines are unlikely to come from late-type stars. More likely, the inner, hidden rim of

the accretion disk suffers funneling of its material onto the massive secondary along magnetic field lines. It could be the source of all sorts of shock heating comparable to pre-main-sequence stars but with a preference in the direction of the orbital motion of the secondary. However, the radiation pressure of the massive star must counteract this accretion process and then must give rise to strong x-ray emission, which is not observed.

5.3.3 Tracing the disk eccentricity

Fig. 12b identifies two atomic-line parameters that apparently relate to the observed disk eccentricity. The top panel shows the transition probability $\log gf$ while the lower panel shows the (lower) excitation potential E_{low} . Line data were again taken from the NIST Atomic Spectra Database. There is the general trend that the transient in spectral lines with higher excitation potential – and thus lower temperature sensitivity – is related to disk regions with higher eccentricity. It thus originates from the outskirts of the disk or even the disk halo and not from the immediate vicinity of the hidden central target.

The dependency on transition probability is more complex (top panel in Fig. 12b). Optically-thick lines like Balmer H I and Ca II irt a.o. solely trace higher eccentricity material and also do so proportional to their transition probabilities. The optically-thin lines show a mixed behavior. Only the low-probability transitions with $\log gf < -1.8$, which are all singly-ionized lines, trace high eccentricity regions, while $\log gf > -1.8$ lines generally trace low-eccentricity regions. Three neutral lines (Fe I 4132, Fe I 4202, Mg I 5172) and three single-ionized lines (Fe II 4924, 5018, 5169) with $\log gf$ between -0.4 and -1.4 trace high-eccentricity material instead. These lines are obviously either very strong (Mg I), are blends of a neutral and a singly-ionized line (5169) or simply have low temperature sensitivity (4132, 4202).

Maintaining the artificial separation at $e \approx 0.2$, we fit two log-linear regressions to the data. These are shown as two straight lines in the top panel in Fig. 12b. Numerically, the fits are

$$\text{for } e > 0.2 : e = +0.036 \log gf + 0.374, \quad (1)$$

$$\text{for } e < 0.2 : e = -0.0154 \log gf + 0.1185, \quad (2)$$

where the constants have errors of ± 0.013 for the case $e > 0.2$ and ± 0.006 for the case $e < 0.2$.

5.4 Evidence for a disk “hot spot”

All line profiles with a disk imprint show increased disk-absorption line broadening at the time when the blue shift is largest, in particular when compared to the time when these lines first appear (see, e.g., Fig. 3b). We measure the average FWHM at the red vertex of the disk rotation profile, i.e. the leading side of the disk, to $8 \pm 2 \text{ km s}^{-1}$ while it is $21 \pm 3 \text{ km s}^{-1}$ at the blue vertex, i.e. the trailing side of the disk (always with respect to the orbital motion of the

secondary star). Such a dispersion would be expected if the disk circumference is significantly non-circular. The extra absorption could be interpreted to be due to the equivalent of a “hot spot” or a “warm region” on that limb of the disk where a mass stream from the F0 primary would reach the disk and where dust grains would be preferably evaporated. The appearance of such extra blue-shifted absorption at the time when that part of the disk that rotates towards the observer is transiting is consistent with an accretion stream that points in the same direction as the rotation of the disk. This was also noticed in the independent study by Griffin & Stencel (2013). However, the stream itself must be mostly hidden from the observer because the dusty part of the disk eclipses its own stream and most of its hot spot. It resembles the typical cataclysmic variable star scenario with a cool donor star and an accreting white dwarf. It also requires that the unseen secondary star is the more massive of the binary system.

Herschel observations confirmed the cool temperature of the disk of 550 K (Hoard et al. 2012) while earlier IR observations revealed 1150 K when that part of the disk was seen that faces the F supergiant. While some of the heating is likely due to the ultraviolet radiation of the F0 star, some of it may be due to the (unresolved) hot spot on the disk. This hot spot, or better “warm region”, should become more and more visible after eclipse due to the increasing aspect angle of the binary after egress. It clearly warrants further monitoring.

6 Photometric analysis

6.1 Introduction

Kim (2008) had used all available out-of-eclipse data from 1842–2006 for a CLEANed wavelet analysis. Two periods were found; 67 d and 123 d. Kloppenborg et al. (2012) followed up on this study with a 27-yr long inter-eclipse *UBV* data set from 81 observers prior to 2,455,000 and also found at least two main periods but with a drift of $dP \approx -1.5 \text{ d/yr}$. They noted that every 3,200 days, about one third of an orbital revolution, the sinusoidal characteristic peaks up. Their predictions for the time of our data matches several of our spectroscopic and photometric periods in Tables 4 and 5. Chadima et al. (2011) found a dominant period of 66.2 d from *UBV* photometry during the recent eclipse, as well as from radial velocities and the intensities of two singly-ionized spectral lines. Additional periods of $\approx 123 \text{ d}$, 270 d and 317 d from a 450-d long time coverage during eclipse were claimed. Even more complex light variations outside of eclipse of up to $0^{\text{m}}15$ in H α and even $0^{\text{m}}20$ in H β were detected from our earlier APT data in 1996–2000 (Strassmeier et al. 2001). The time coverage for the H α photometry was two consecutive observing seasons and one full observing season for H β but with high sampling throughout the season. Its period analysis yielded five significant periods with the largest amplitudes at periods of 78.9 d and

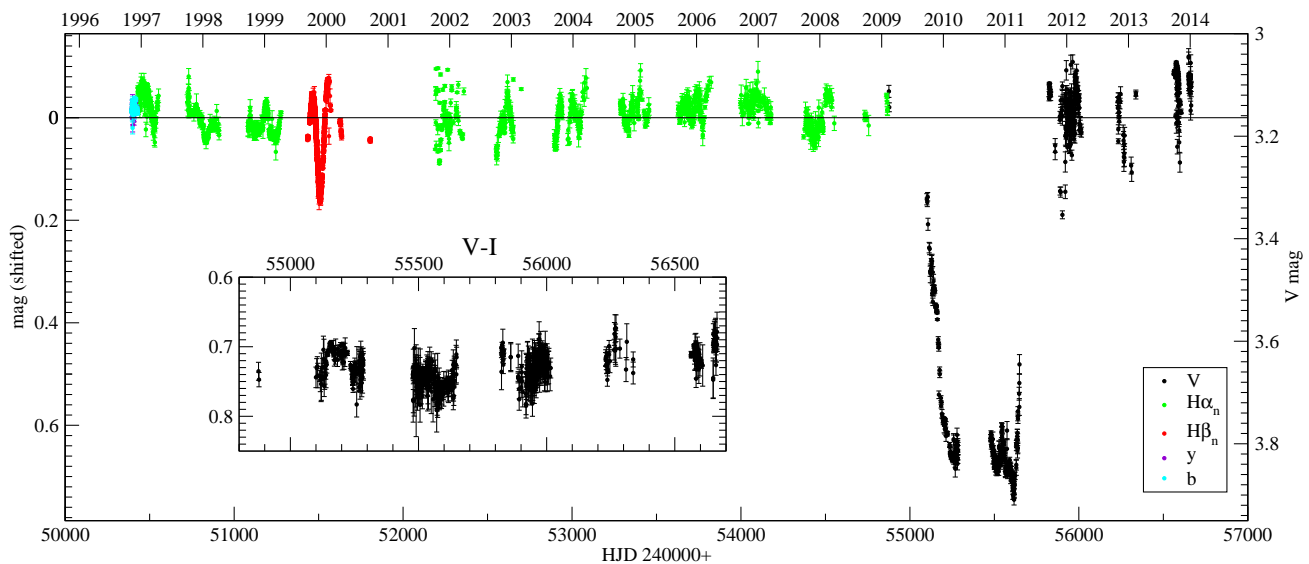


Fig. 13 Amadeus APT photometry from 1996-2013. Colors, or gray tones, identify different filters as indicated in the small insert. The large insert shows the $V - I$ color data inside and outside of eclipse. The eclipse is seen in the right part of the graph. The right axis is V magnitude, the left axis is bandpass-specific magnitudes after shifting to the long-term average (solid horizontal line).

130 d, and eight periods for $H\alpha$ with the largest amplitudes at 132 d, 89 d and 73 d.

6.2 Period search

Fig. 13 shows our entire APT data from 1996 until 2013, covering a total of 6,300 d. The data gaps are the seasonal gaps except in the season 2000/01 when the *Amadeus* APT was oversubscribed.

6.2.1 From $H\alpha$ narrow band

$H\alpha$ narrow band constitutes our longest homogeneous data record for ϵ Aur. It covers 4,438 d with a total of 1,100 data points with an internal error better than 0^m01 . Only out-of-eclipse data are available. We first examined each observing season separately with *period04* (Lenz & Breger 2005) and found a jump in the zero point from 3^m164 before to 3^m226 after JD 2,453,500, i.e. three years before the eclipse. Its origin is an instrumental offset and we correct for it by simply shifting the seasonal means to the long-term mean. The corrected data set is then used for the period search with short-term Fourier transforms.

Fig. 14 shows the result from $H\alpha$. We again applied the same program package TiFrAn (Kolláth & Oláh 2009) for non-stationary time series as we did for the line-profile variability in Sect. 5.1.3. Note that the periods in this figure can be directly compared with the spectroscopic $H\alpha$ tracers, e.g. the radial-velocity variations in Fig. 10c, at least for the time with overlap after JD 2,454,000. The two main spectroscopic $H\alpha$ periods were ≈ 116 d from the line core and ≈ 150 d from the center-of-intensity radial velocities. The comparable photometric $H\alpha$ periods are 101.7 d and 139.2 d. Other photometric periods of around 81 d, 68 d, and 42 d may have been present at earlier times predating

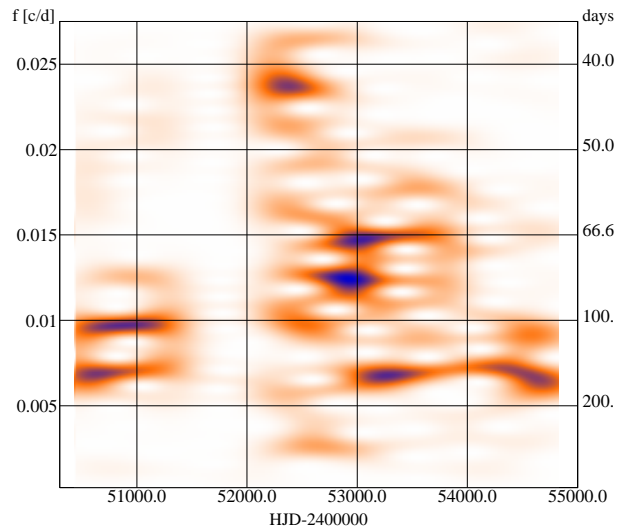


Fig. 14 Time-frequency distribution of the $H\alpha$ narrow-band photometry from short-term Fourier transforms.

our spectroscopic record. The most persistent frequency appears to be the mode at $P \approx 139$ d, which is visible during the entire photometric data set. It appears that this period is waxing and waning with time rather than linearly drifting. Note that there were no observations around JD 2,452,000, accounting for the lack of signal at that time. The existence of a peak at 1,618 d verify that some sort of a long-term modulation is present, which may be related to the twice-as-long 3,200 d cycle reported by Kloppenborg et al. (2012). A plain Lomb periodogram confirms this with a very significant peak at a slightly longer but consistent period of 1,630 d.

Table 5 Results from the photometric period analysis. Periods are arranged according to their significance.

n_f	f (d^{-1})	P (d)	Amp. (mmag)	S/N
<u>From $H\alpha$</u>				
1	0.00365	274 \pm 1.5	12.8 \pm 1.7	10.1
2	0.000618	1618 \pm 32	16.7 \pm 1.7	9.9
3	0.00718	139.2 \pm 0.4	17.1 \pm 1.8	7.6
4	0.00984	101.7 \pm 0.3	12.5 \pm 2.4	7.4
<u>From $H\beta$</u>				
1	0.01292	77.48 \pm 0.04	67.70 \pm 0.11	208
2	0.00753	132.28 \pm 0.14	58.43 \pm 0.14	180
3	0.02910	34.53 \pm 0.06	3.84 \pm 0.08	11.5
<u>From Johnson V</u>				
1	0.011768	85.0 \pm 0.2	28.3 \pm 1.8	31
2	0.013662	73.2 \pm 0.2	14.6 \pm 1.6	16
3	0.007455	134.1 \pm 0.9	11.1 \pm 1.1	12
4	0.025046	39.9 \pm 0.1	9.1 \pm 1.2	10
<u>From Johnson I</u>				
1	0.011847	84.4 \pm 0.2	26.8 \pm 8.4	24
2	0.007332	136 \pm 22	15.0 \pm 8.5	14
<u>From combined $H\beta$ & V</u>				
1	0.01295	77.2349 \pm 0.0006	66.02 \pm 0.04	172
2	0.00754	132.610 \pm 0.002	57.04 \pm 0.06	150
3	0.02884	34.6806 \pm 0.0006	8.07 \pm 0.05	20.5
4	0.02395	41.7657 \pm 0.0009	4.70 \pm 0.05	12.2
<u>From all data</u>				
1	0.007589	131.77 \pm 0.15	33.3 \pm 1.9	77
2	0.010992	90.97 \pm 0.04	28.2 \pm 2.1	65
3	0.012888	77.59 \pm 0.11	25.9 \pm 1.4	60
4	0.012192	82.02 \pm 0.11	17.8 \pm 1.7	41
5	0.013517	73.98 \pm 0.07	12.5 \pm 1.5	29
6	0.005721	174.8 \pm 1.0	10.6 \pm 1.7	24
7	0.031986	31.26 \pm 0.02	4.9 \pm 1.0	11
8	0.023776	42.06 \pm 0.02	4.5 \pm 1.0	10

6.2.2 From $H\beta$ narrow band

A careful re-examination of the $H\beta$ narrow-band data obtained with the Wolfgang APT (T6) in September 2000 allowed us to reclaim 38 more data points than in our original publication (Strassmeier et al. 2001). These data clustered 168.4 d later than in the original data. It increased the time base and allowed us to re-determine the $H\beta$ periods with increased precision. The results are summarized in Table 5. The two dominant periods were 77.5 d and 132.3 d. The analysis was done with *period04* for all frequencies down to $S/N > 6$ but a fourth period with $S/N = 6.3$ of 24.6 d is rejected. The most-likely errors for the periods and amplitudes were deduced by a Monte-Carlo method on 10,000 synthetic data sets following the procedure outlined and applied in Strassmeier et al. (2012).

6.2.3 From Johnson-Cousins V and I band

From a total of 1,247 data points in V and I , only measurements with an internal error of less than 6 mmag in V and 8 mmag in I were used for the period analysis. This criterion

limited the available data points to just 103 (106 in I) for out-of-eclipse, and to 121 (126 for I) for the in-of-eclipse phase. It just demonstrates that broad-band photometry of a third magnitude star is not without troubles. In general, data quality within eclipse was lower than out of eclipse, which resulted in higher error bars on its periods and amplitudes.

The *period04* analysis of the out-of-eclipse V -band data shows two main periods, one at 76.9 \pm 0.1 d and one at 142.4 \pm 1.3 d with amplitudes of 46.9 \pm 1.6 mmag and 21.0 \pm 1.8 mmag, respectively. Five outliers with a deviation of $> 3\sigma$ were deleted. The same analysis for the out-of-eclipse I -band data gave 77.8 \pm 0.2 d and 144.9 \pm 1.4 d with amplitudes of 28.5 \pm 1.9 mmag and 20.5 \pm 2.6 mmag, respectively. Four outliers were removed. We consider the V and I periods equal to within their estimated errors.

The in-of-eclipse V and I data was searched for similar periods. In V , periods of 84.2 \pm 1.1 d and 195.4 \pm 14.5 d with amplitudes of 26.1 \pm 1.6 mmag and 14.9 \pm 2.5 mmag, respectively, could be confirmed. In I , it was 86.0 \pm 6.1 d and 177 \pm 80 d with amplitudes of 19.4 \pm 3.9 mmag and 6.8 \pm 5.3 mmag, respectively. This decrease of period from in-of-eclipse to out-of-eclipse is consistent with the period changes derived from spectroscopic data.

Next, we combine the in-of-eclipse and the out-of-eclipse data sets by shifting V and I by their respective zero-point differences of 0^m700 and 0^m676. Note that the 24 mmag difference between the zero-point offsets between V and I is just at the 3- σ level. We still call the eclipse color “neutral”. The *period04* analysis of the combined data set in V now shows four frequencies with a $S/N > 10$ rather than just two. Employing the generous $S/N > 4$ criterion (Breger et al. 1993) leads to many, likely spurious, detections and a cut off at $S/N > 10$ is adopted instead. The same analysis was done with the I -band data but only two frequencies with $S/N > 10$ could be verified (Table 5). Neither of the two longer periods from the in-of-eclipse set, 195 d in V and 177 d in I , could be verified, while the two shorter periods were clearly seen in the combined sets.

6.2.4 From the combined data

We also attempted to analyze the grand combined data set by shifting all passbands to their respective zero points, again determined seasonally with *period04*. An analysis of this data with TiFrAn showed only the frequencies dominant in $H\beta$ and in VI , almost completely blanking out the periods found from $H\alpha$. This is not surprising given the large amplitude in $H\beta$ and VI compared to $H\alpha$ in combination with its non-overlapping time distribution. The time-average periodogram with *period04* reveals a total of eight frequencies with $S/N > 10$ that appear to be better constrained than from the individual passbands. Combining only the two data sets with large amplitudes, $H\beta$ and V of 2,236 usable data points including proper shifts of the in-eclipse data, yields two dominating but altogether four significant periods of 132.6 d, 77.2 d, 34.7 d and 41.7 d. Because the $H\beta$ and the V -band data are from epochs 10 years

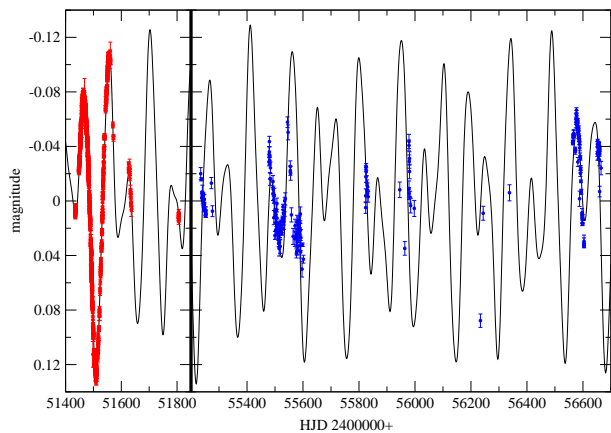


Fig. 15 Phase coherence of the $H\beta$ photometry (left part, red dots) and the V -band photometry (right part, blue dots). The line is the combined $H\beta$ & V period solution from Table 5. Note that the vertical separator line represents a data-free window between the $H\beta$ data and the V data of 3,450 days.

apart, from 2000 for $H\beta$ and 2010+ for V , the four-period solution is remarkably phase coherent (Fig. 15). This would be expected if the periods are due to a (non-radial) oscillation pattern. All results are listed again in Table 5.

6.3 The 2009-2011 eclipse

The average eclipse depth in the V band was 0^m700 . The $V - I$ index remained nearly constant with an average $V - I$ of 0.74 ± 0.02 mag inside as well as outside of eclipse. The insert of Fig. 13 shows the general color neutrality during eclipse. Some short-term variations are attributable to the F0-star pulsations. Unfortunately, the seasonal gap fell right within the mid of eclipse and no statement with respect to central brightening can be made from our data. A periodogram analysis of the $V - I$ data within the eclipse revealed no significant periods, though a variability of 0^m02 is seen.

6.4 Interpretation

We interpret the narrow-band (31 Å) $H\alpha$ brightness to be a composite from at least three different physical origins. Firstly, it is modulated by the supergiant non-radial pulsation pattern, just like we have seen from the line profiles. Secondly, the stellar wind and environment of the F0 supergiant may not be homogeneous all the time which, thirdly, also applies to the mass accretion stream and the extended accretion-disk halo. This would explain why the photometric amplitudes in $H\alpha$ are smaller (by a factor of two) than in $H\beta$ and its periods not always identical.

The variations of the $V I$ as well as the $H\beta$ photometry are likely dominated by stellar pulsation. A periodogram analysis of the merged $H\beta$ and V data set suggests a phase coherence over an interval of 5,300 d (Fig. 15). Its two main periods are 132 d and 78 d. It also reveals that the frequency

of 0.0291 (34 d) in the $H\beta$ set is split into two at 34.7 d and 41.7 d.

7 The visual components of the ϵ Aur multiple star system

7.1 Absolute parameters

According to the Aitken Double Star catalog (Aitken & Dolittle 1932) ϵ Aurigae is a possible quintuple star system. As already mentioned by Guinan et al. (2012) all of these putative components could be foreground or background field stars. We have therefore obtained high-resolution spectra for all of them. Components B, C, and D are all faint and within less than one arc min from the bright A component (ϵ Aur = ADS 3605A) while component E (BD+43° 1168) is a 9.4-mag star 3.4 arc min away. Proper motions (p.m.) are only known for ϵ Aur (p.m. $\alpha/\delta = -0.86/-2.66$ mas/yr) and for BD+43° 1168 ($-1.3/-2.1$ mas/yr).

Table 6 summarizes the stellar components. Coordinates are from FK5 and proper motions from Tycho-2 (Hog et al. 2000) except for ϵ Aur itself which are from *Hipparcos*.

ADS 3605B. This 14th-mag star is just 28'' away from ϵ Aur. Nothing is known except the position and an approximate brightness. Our NOT/FIES spectrum has a S/N ratio of 40:1 (90 min exposure) and shows an almost featureless spectrum besides $H\alpha$. A few very weak lines are detected though. Notable are Si II 6347 (150 ± 20 mÅ) and 6371 (< 50 mÅ), shown in Fig. 16, while other lines are present but unidentified, e.g. $\lambda 6270$ (?), $\lambda 6823$ (?), $\lambda 5582$ (?). Two more lines are seen near 6700 Å; one at $\lambda 6698.7$ (?) and one at $\lambda 6706.1$ (?). No He I lines at 5876 or 6678 are seen. The Na D_{1,2} V- and R-component ISM lines (see Münch (1957) are resolved and both saturated, like in ϵ Aur. A third ISM component (EW ≈ 40 mÅ) in both lines appears resolved and redshifted by 13.3 km s^{-1} . No photospheric Na D_{1,2} absorption is seen. The DIB lines at $\lambda 6613$, 5780, and 5797 are among the strongest non-H lines in its spectrum and are clearly detected (Fig. 16, Table 6). The $\lambda 6613$ EW would suggest a distance of 2 kpc if the calibration by Guinan et al. (2012) were valid.

While no match was found with any of the ESO UVES archive spectra (Bagnulo et al. 2003), a good match of $H\alpha$ was found with the spectra of two cool white dwarfs (NLTT 32785 and 56493) from the sample of Kawka & Venners (2012). Equivalent widths for Balmer $\alpha\beta\gamma\delta$ are measured from our one spectrum to 10.0, 9.1, 7.2, and 6.6 Å, respectively. We conclude that BD+43° 1166B is a cool DA white dwarf, $T_{\text{eff}} \approx 5,000 - 7,000$ K and $M_V \approx 14^m8$, with weak metallic lines. Its distance is then ≈ 7 pc, instead of 2 kpc (!) from the $\lambda 6613$ DIB line, and thus unrelated to the ϵ Aur system. This suggests that the white dwarf has a debris disk that causes the DIB lines.

ADS 3605C. Our spectrum indicates a K3-4 MK-class III giant from the spectrum morphology and from various line-depth ratios in the 6450-Å region (see Strass-

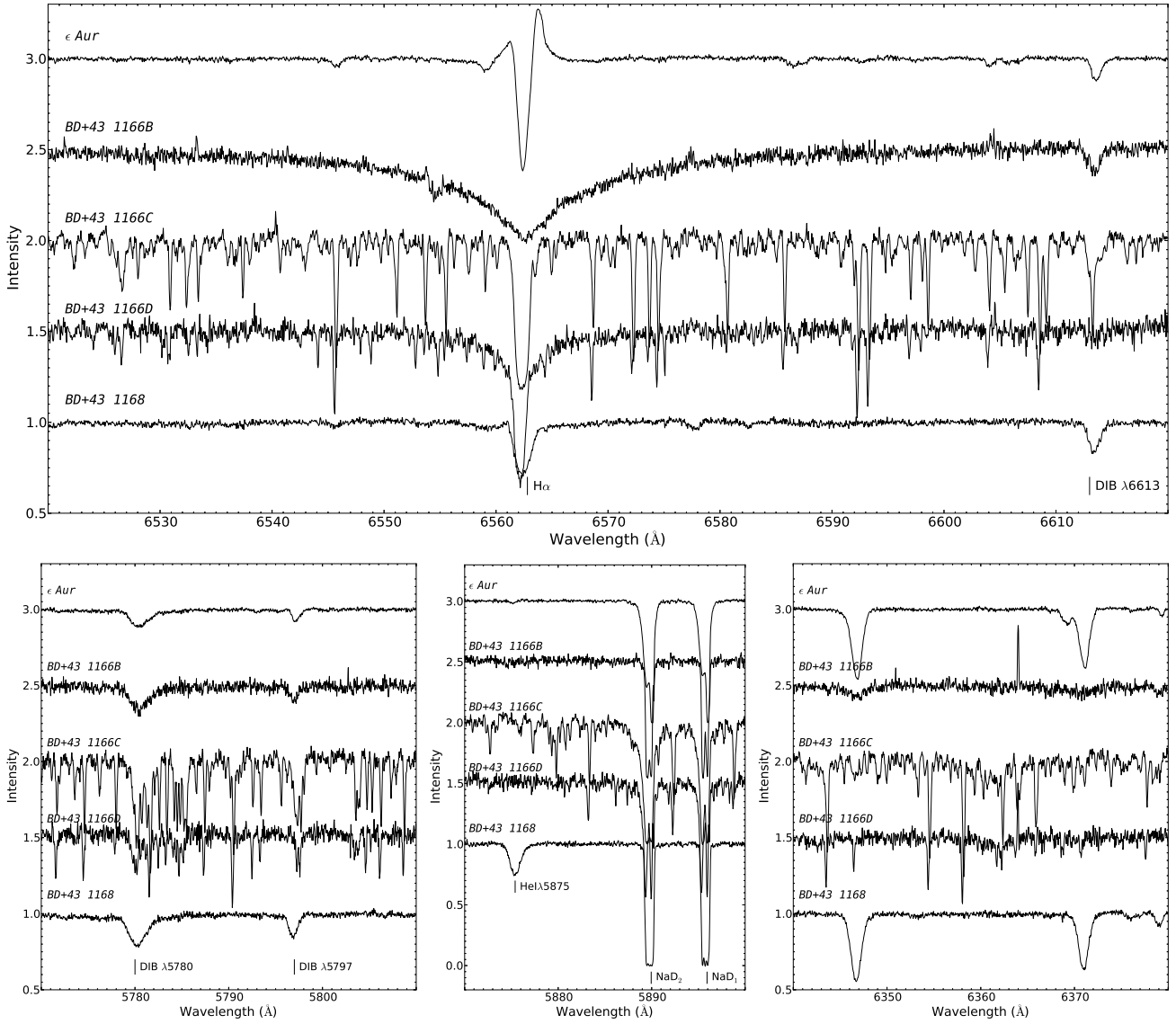


Fig. 16 Selected spectral regions of the bonafide ADS3605 components. Spectra shown from top to bottom: ϵ Aur (BD+43° 1166A), BD+43° 1166B, BD+43° 1166C, BD+43° 1166D, and BD+43° 1168. Top panel: Balmer H α and the λ 6613 DIB line. Bottom left: the two DIB lines at λ 5780 and λ 5797. Bottom middle: Na D $_{1,2}$ lines and He I 5875. Bottom right: the two Si II lines λ 6347 and λ 6371.

Table 6 The ADS 3605A-E bonafide quintuple system.

Name	V (mag)	RA (2000) (h m s)	DEC (° ' ")	Sp.	$m - M$ (mag)	v_r (km s $^{-1}$)	λ 5780 DIB line EW in (mÅ)	λ 5797 DIB line EW in (mÅ)	λ 6613 DIB line EW in (mÅ)
A ϵ Aur	3.1	05 01 58.1	+43 49 24	F0Ia	+10.9 ± 0.9	-2.26 ^a ± 0.15	285 ± 5	77 ± 2	128 ± 3
B BD+43° 1166B	14.0	05 01 56.6	+43 49 08	cDA	-0.8 ± 0.5	-14.6 ± 0.9	340 ± 20	100 ± 10	140 ± 10
C BD+43° 1166C	10.9	05 01 54.0	+43 49 26	K3-4III	+10.9 ± 1	-23.71 ± 0.04	200 ± 50	100 ± 50	110 ± 10
D BD+43° 1166D	12.0	05 01 55.1	+43 49 57	G8V	+6.4 ± 0.3	-30.47 ± 0.02	50 ± 20	30 ± 20	35 ± 10
E BD+43° 1168 ^b	9.4	05 02 12.4	+43 51 42	B9Iab	+15.7 ± 1	-22 _v ± 0.07	495 ± 10	180 ± 7	196 ± 7

^aCenter-of-mass velocity from Stefanik et al. (2010).

^bRadial velocity is variable, see text.

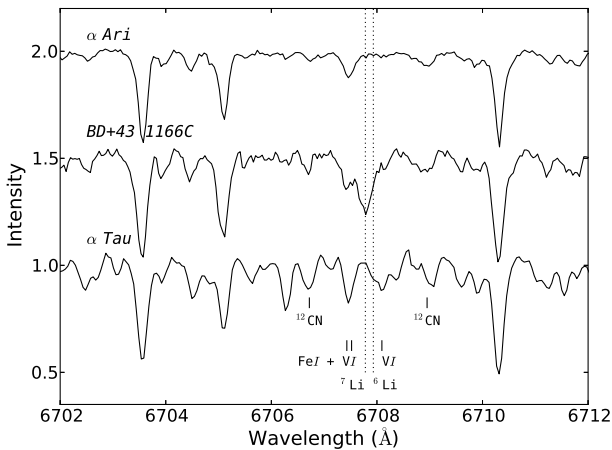


Fig. 17 The lithium $\lambda 6708$ region for BD+43°1166C (middle spectrum). Shown are two comparison spectra of the nearby giants α Ari (K2III, top) and α Tau (K5III, bottom). The top two spectra are shifted in intensity for a clearer display.

meier & Fekel 1990). A spectrum-synthesis solution yields $T_{\text{eff}}=4,470$ K, $\log g=2.8$, $v \sin i=3.6$ km s $^{-1}$ and solar metallicity. The rotational broadening from the full-width half maxima of a subset of weak spectral lines is $v \sin i=4\pm 1$ km s $^{-1}$, adopting a macroturbulence of 3 km s $^{-1}$ from Gray (2005), in good agreement with the synthesized value. Interestingly, we detect a Li I 6708-Å line with an EW of 80 mÅ. It converts into an abundance of $\log n(\text{Li})=1.35\pm 0.10$ ($\log n(\text{H})=12$) from the NLTE tables in Pavlenko & Magazzu (1996). Differential *UBV* observations of this star secured at Hvar Observatory (12 individual observations in 5 nights) gave $V = 10^{\text{m}}93\pm 0.09$, $B - V = 0^{\text{m}}71\pm 0.02$, and $U - B = 0^{\text{m}}32\pm 0.01$ (Guinan et al. 2012). However, $B - V = 1^{\text{m}}83$ was given in Lutz & Lutz (1977). Neither of these colors fit a K3-4 giant, which probably just indicates the difficulty doing multi-color photometry for a faint star 45'' away from a really bright star. Gray (2005) lists an absolute magnitude of $+0^{\text{m}}2$ for K3-4III which converts, with above Hvar brightness, to a modulus $m - M$ of $+10^{\text{m}}7$. However, the K5III MK-standard α Tau has a measured radius of 44 R_{\odot} (Richichi & Roccatagliata 2005) that converts to an absolute magnitude of $-0^{\text{m}}4$ and thus brighter by $0^{\text{m}}4$ than what is listed in Gray (2005) for K5III. Therefore, we could expect also a brighter absolute magnitude for K3-4, say $0^{\text{m}}0\pm 0^{\text{m}}2$, and get a modulus of $+10^{\text{m}}9\pm 0^{\text{m}}2$ for BD+43°1166C. All of these cases are within the errors bars and practically identical to the modulus for ϵ Aur.

Table 6 lists equivalent widths for the DIB lines at $\lambda 5780$, 5797, and 6613 Å. Measuring these lines in cool-star spectra is difficult due to the blending with numerous photospheric lines. Therefore, we first removed a spectrum of a very bright, i.e. nearby, star of similar classification and presumably no DIB contribution and then measured the DIB lines from the residual spectra. We used an average of α Ari (K2III, $d=20.1$ pc; van Leeuwen 2007) and α Tau (K5III, $d=20.4$ pc; van Leeuwen 2007). The $\lambda 5780$ and $\lambda 5797$ regions are severely more blended than the $\lambda 6613$ line (cf.

Fig. 16) and the EWs are accordingly uncertain. Our best value for EW($\lambda 6613$) is 110 ± 10 mÅ which would place the star at a distance of 1.6 ± 0.1 kpc according to the calibration in Guinan et al. (2012). We note that the error of 10 mÅ for the EW is just a rms from repeated measurements and could be much larger, in particular when the expected calibration error would be added.

ADS 3605D. This star is 47'' away from ϵ Aur. Our spectrum indicates a G8 dwarf, again from the spectrum morphology and various line-depth ratios in the 6450-Å region as well as the H α wings. A spectrum-synthesis solution yields $T_{\text{eff}}=5090$ K, $\log g=5.0$, $v \sin i=2.3$ km s $^{-1}$ and $[\text{Fe}/\text{H}]=-0.06$. Its rotational broadening is barely detected with the given spectral resolution ($R=47,000$) and could be ≤ 2 km s $^{-1}$ (expecting a macroturbulence of also 2 km s $^{-1}$). No lithium 6708 line ≥ 5 mÅ is detected. With M_V of $+5^{\text{m}}6$ from Gray (2005), the modulus becomes $+6^{\text{m}}4$. The star must be in the foreground at a distance of ≈ 170 pc (adopted $A_V = 0^{\text{m}}2$) and thus not related with ϵ Aur. We used a G8V template spectrum (HD 171067, see Strassmeier et al. 2012) for subtraction from BD+43°1166D in order to obtain the DIB equivalent widths listed in Table 6. The $\lambda 6613$ EW suggests a distance of ≈ 500 pc if the Guinan et al. (2012) calibration is applied.

ADS 3605E = BD+43°1168. Van de Kamp (1978) used it as one of his reference stars for the parallax measure on ϵ Aur. He listed it as a G0-star with m_v of 9 $^{\text{m}}6$. Münch (1957) had measured two ISM components, dubbed the V- and R-component, in NaD and Ca II H&K and listed radial velocities of -18 and 0 km s $^{-1}$ for the two components, respectively, but with large uncertainties and probably unresolved. He lists the spectral type as B9Iab and measured a heliocentric RV of the star of -22 km s $^{-1}$. Three STELLA spectra gave velocities of -23.115 ± 0.029 km s $^{-1}$ (2,456,625.580527), -20.818 ± 0.068 km s $^{-1}$ (2,456,601.640161) and -22.740 ± 0.030 (2,456,708.473611) indicating low-amplitude variability. Guinan et al. (2012) measured a 6613-Å DIB equivalent width of 230 ± 20 mÅ (200 mÅ was listed by Bromage & Nandy 1973) and $E(B - V)$ of $0^{\text{m}}90$ and concluded on a distance of 3440 ± 170 pc based on the apparent V magnitude of 9 $^{\text{m}}4$.

Our spectra are in agreement with this distance and show a fully saturated Na D doublet, a blue-shifted Ca II-H ISM line, and strong DIB lines at $\lambda 5780$, 5797, and 6613 Å. No photospheric Na D $_{1,2}$ absorption is seen. The K I 7699 line appears also very strong and with a profound triplet profile, like Na D. The DIB EWs are on average a factor two larger than those for ϵ Aur. The star shows strong He I $\lambda 5875$ (327 ± 10 mÅ) and $\lambda 6678$ -Å (250 ± 10 mÅ) lines. As already mentioned, ϵ Aur shows only a very weak He I-5875 absorption with 11.7 mÅ, none of the other ADS-3605 stars do. The two Si II lines around 6360 Å are as prominent as in ϵ Aur and support the B9 supergiant classification. Several weaker lines remain unidentified, e.g. Fe II (?) 6456, or $\lambda 7065$, $\lambda 5640$, or $\lambda 5849$. As already mentioned by Guinan

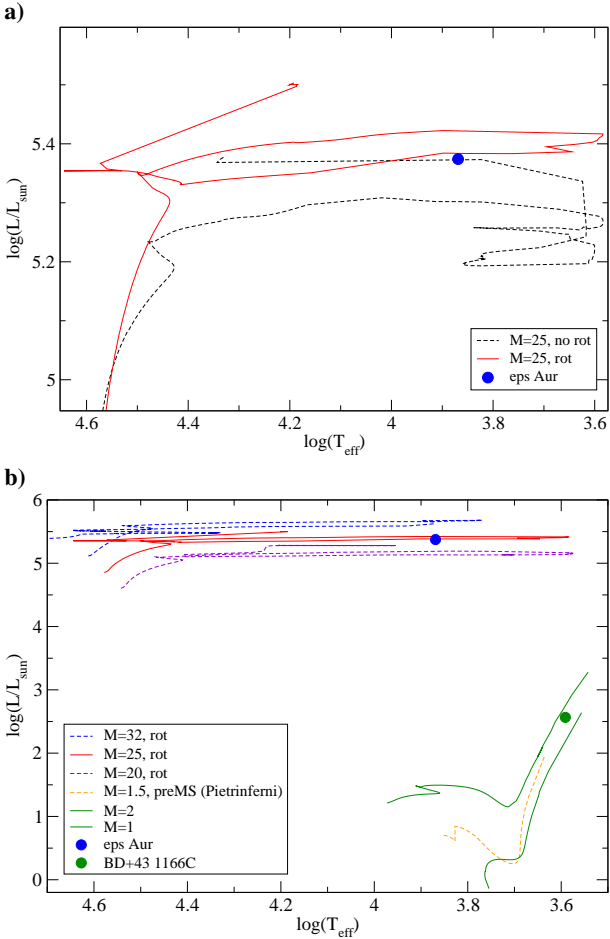


Fig. 18 H-R diagrams of the two bona-fide visual ϵ Aurigae components A and C with tracks from Ekstroem et al. (2012). **a** A comparison with the position of ϵ Aur. The full line is a 25- M_{\odot} rotating model, the dashed line a 25- M_{\odot} non-rotating model. Others are indicated in the insert. **b** A comparison with the position of BD+43° 1166C. Highlighted are a 1- and a 2- M_{\odot} non-rotating model for BD+43° 1166C and three models for ϵ Aur (see insert).

et al. (2012) $H\alpha$ appears very weak. Our spectra clearly show a blue-shifted emission component that indicate the typical supergiant wind, again like in ϵ Aur. We measure a $H\alpha$ -core equivalent width of 510 mÅ and a $H\gamma$ equivalent width of 2.64 Å. With the calibration of absolute magnitude versus $H\gamma$ for O6–A3 supergiants by Petrie (1966), we obtain $M_V = -6^m3$ and thus $m - M = +15^m7$. This verifies that BD+43° 1168 is not related with ϵ Aur but is a background star at ≈ 3 kpc as judged from the strength of the DIB lines.

7.2 Summary: binary membership

Our main result from the previous subsection is that only BD+43° 1166C could be a gravitationally bound component with ϵ Aur. The other bona-fide ADS 3605 components are either foreground or background stars. The upper and lower limits of the distance to BD+43° 1166C would be 1.8 kpc if $A_V = 0$ and $M_V = -0^m4$ (from α Tau) and 900 pc if $A_V =$

1^m12 based on the average measured $E(B - V) = 0^m35$ from Guinan et al. (2012) and $M_V = 0^m0$ from Gray (2005), respectively. Note that the DIB $\lambda 6613$ -line EW suggests ≈ 1.6 kpc with the calibration from Guinan et al. (2012). Given the comparably large EW errors for DIB lines in late-type spectra, the EW value for BD+43° 1166C is still consistent with the EW of ϵ Aur. However, the three DIB EW values for the other components in Table 6 are not consistent with each other if a single distance calibration shall apply. Most notably, the close-by white dwarf BD+43° 1166B has negative $m - M$ but larger DIB EWs than ϵ Aur. This just proves that circumstellar material can and will dominate the strength of these lines. We conclude that the most likely value for the distance to BD+43° 1166C is with $A_V = 1^m12$ and $M_V = 0^m0$, thus 900 pc. We adopt this value also for the distance to ϵ Aur.

At this distance, the on-sky separation of BD+43° 1166C from ϵ Aur of $44.77''$ translates to roughly 40,300 au. Thus, for a bound orbit, the velocity difference between the respective center of masses may not exceed 1.5 km s^{-1} . In case the proper motions of ϵ Aur and BD+43° 1166C would be equal (the latter p.m. is not known) this velocity difference is also the maximal allowed difference of the center-of-mass velocities. Then, a circular orbit would have a period of 1 Myr for a sum of the masses of all three components of $50 M_{\odot}$ (or 1.56 Myr if the mass sum is more like $20 M_{\odot}$).

BD+43° 1166C's measured radial velocity is -23 km s^{-1} , and thus 20 km s^{-1} different to the systemic center-of-mass velocity of the ϵ Aur binary ($-2.26 \pm 0.15 \text{ km s}^{-1}$; Stefanik et al. 2010). If we assume that it is not a close binary itself, we conclude that even BD+43° 1166C is not physically connected to ϵ Aur despite that is roughly at the same distance. Consequently, we suggest to drop the ADS3605A-E entry from any visual-binary list.

8 Discussion and summary

The interferometric (uniform-disk) diameter of the F0-supergiant, $2.10 \pm 0.04 \text{ mas}$ ($\lambda 1.6 \mu\text{m}$; Kloppenborg et al. 2010) and $2.10 \pm 0.02 \text{ mas}$ ($\lambda 660 \text{ nm}$; Mourard et al. 2012), suggests a stellar radius of between 140–340 R_{\odot} if at distances between 625–1500 pc, respectively. Our new effective temperature of $7395 \pm 70 \text{ K}$ constrains the plausible range for its logarithmic luminosity to 4.7–5.5 L_{\odot} ($M_V = -7^m0$ to -8^m9). In any case, this is the classic blue supergiant region in the H-R diagram. Evolutionary tracks would place the star very close to the point where the central helium content is already exhausted and C-ignition could have already happened.

With ϵ Aur today's $\log L/L_{\odot} = 5.37$ (from $d = 900 \text{ pc}$ and $R \approx 300 R_{\odot}$) and $\log T_{\text{eff}} = 3.87$, the $Z = 0.014$ rotating models of Ekstrom et al. (2012) with prescribed mass loss suggest an initial (ZAMS) mass for the F-star of $\approx 25 M_{\odot}$ (Fig. 18a). An initial rotation of 40% of the break-up velocity was adopted. Note that a similar non-rotating

model is always less luminous and therefore would suggest a slightly higher mass. Given the luminosity, the radius, T_{eff} and $\log g = 1$ the expected mass from the Stefan-Boltzmann relation is $\approx 30 M_{\odot}$. The tracks have three horizontal branches. If on the first ascent ϵ Aur would have an age of 8 Myr and still a mass of $23.5 M_{\odot}$. If after He-ignition (at the low- T_{eff} turnaround) the age would be 8.2 Myr and the mass more near $13.1 M_{\odot}$. A direct comparison with tracks remains inconclusive though because of the uncertainty of the mass-loss history in the models (see Martin & Palacios (2013) for a comparison of high-mass tracks). However, the most critical uncertainty is due to the binarity of ϵ Aur and the fact that there is an accretion disk around the secondary star that is fed by the F-star. Therefore, the initial mass loss from the F-star might have been considerable different than the prescribed mass loss in the models. For a low-mass track of initial mass of, say, $\approx 7 M_{\odot}$ the effective temperature on the other hand is too high for the star to be in the post-AGB phase, but possibly could be reached if there was a large initial mass transfer between the primary and secondary.

Out of the four bona-fide ADS 3605 components only ADS 3605C = BD+43° 1166C appears at the same distance as ϵ Aur. Its logarithmic luminosity in solar units is 3.59 and the effective temperature ≈ 4250 K. However, its radial velocity is 20 km s^{-1} off the expected velocity if it were gravitationally bound to ϵ Aur. We conclude that the bona-fide ADS3605A-E visual quintuple system does not exist as such. Fig. 18b shows a H-R diagram with single-star tracks that fit ϵ Aur and BD+43° 1166C, respectively. No joint isochrone is possible according to the single-star tracks shown. While the F-supergiant of ϵ Aur would be 10 Myr of age, BD+43° 1166C would be 6 Gyrs of age. One would conclude that the two components can not be coeval. We take this as further evidence that the current evolutionary status of the close binary system had been shaped by mass exchange in the past.

The continuity of our time-series line profiles allowed us to separate the effects of pulsation and rotation. With the assumption that the rotational line broadening would not change over time, we find a projected rotational velocity $v \sin i$ of $28 \pm 3 \text{ km s}^{-1}$. Its residuals over time exhibit a clear period of 62.6 ± 0.7 d, which we interpret to be the main pulsation period. Note that if this period were the rotational period instead, the $v \sin i$ of 28 km s^{-1} implies a minimum radius of $34.6 R_{\odot}$ in obvious contradiction with the interferometric radius of at least $140 R_{\odot}$. Combined with above T_{eff} it would result in a luminosity of just $3200 L_{\odot}$, or a distance of just 250 pc if we assume no interstellar absorption. This distance appears significantly closer than any of the distance measurements and must be rejected. Therefore, the 62.6-d period is not the rotation period but most be one of the many pulsation periods. It is also possible that this period is the same as the 67-d period found by Kim (2008) from long-term photometry. The most likely rotation period of ϵ Aur can be estimated from R and $v_{\text{rot}} \sin i$.

With $R=300 R_{\odot}$ from $d=900$ pc and a rotational velocity of 28 km s^{-1} (with $i = 89^{\circ}$), a rotational period of $P=540$ d follows. Its range of equal likeliness is 250-614 d. For a supergiant, a 540-d period is still “rapidly rotating” though.

Our echelle spectra enabled us to extract the disk-rotation profile from a large variety of spectral lines. Firstly, we found that transient absorption lines group into two profile families, ones with high eccentricity ($e > 0.2$) and ones with low eccentricity ($e < 0.2$). Secondly, this bi-modality is also established from the line transition probabilities and excitation potentials and indicate that the high $\log gf$ and high E_{low} lines generally trace high-eccentricity material. Thus, it originates from the leading periastron section of the disk or even the disk halo, while the low $\log gf$ and low E_{low} lines generally trace low-eccentricity material and thus are likely from material just more evenly distributed among the disk. The fact that the Balmer line profiles show variability mostly in their red wings is in agreement with this scenario. No direct spectral evidence is found for the hidden secondary star. We interpret the increased velocity dispersion of the absorption-disk lines during egress due to a hot (or warm) spot on the trailing section of the disk.

Finally, a reanalysis of all our new and previously-published photometry revealed a rich spectrum of oscillation periods from the F0 supergiant. The two main periods were found from $H\beta$ and Johnson V and I and are 77 d and 132 d. Note that the residual average line broadening of optically-thin lines showed a period of 62.6 d, in particular at egress and after the eclipse. Line-profile variability had the most-significant periods at ≈ 110 d, 74 d, and 64 d (with errors of ± 3 d). Radial velocities also showed the 110-d period among others. The two main spectroscopic $H\alpha$ periods, ≈ 116 d from the line core and ≈ 150 d from the center-of-intensity radial velocities, may have a counterpart in the 102 d and 139 d in the $H\alpha$ photometry. Besides, the $H\alpha$ photometry revealed two very long periods of 274 d and 1618 d likely related to a beat phenomenon of the time-variable oscillation pattern of the supergiant. However, $H\alpha$ remains difficult to interpret due to several contributing sources; the F0 chromosphere and wind, the disk accretion stream, and the disk and its halo itself.

Acknowledgements. The STELLA project is funded by the Science and Culture Ministry of the German State of Brandenburg (MWFK) and the German Federal Ministry for Education and Research (BMBF). It is a pleasure to thank Robert Stencel, Elizabeth Griffin and Petr Harmanec for communicating their papers prior to publication and to Ansgar Reiners and Ed Guinan for several discussions regarding the nature of the multiple system. We also thank an anonymous referee for a very helpful and competent report that improved the paper. LS is grateful to Othmar Stahl for the conversion of the original echelle spectra into a MIDAS readable format.

References

Abt, H. A., & Morrell, N. I. 1995, *ApJS* 99, 135

- Aerts, C., Puls, J., Godart, M. & Dupret, M.-A. 2009, *A&A* 508, 409
- Aitken, R. G., & Doolittle, E. 1932, *New general catalogue of double stars within 120° of the north pole*, Carnegie institution of Washington, Washington, D.C., Pub. 417
- Allende-Prieto, C. 2004, *AN* 325, 604
- Bagnulo, S. E., Jehin, E., Ledoux, C., Cabanac, R., Melo, C., & Gilmozzi, R. 2003, *The Messenger* 114, 10
- Breger, M., Stich, J., Garrido, R. et al. 1993, *A&A* 271, 482
- Bromage, G. E., & Nandy, K. 1973, *A&A* 26, 17
- Budaj, J. 2011, *A&A* 532, L12
- Cameron, A. G. W. 1971, *Nature* 229, 178
- Castelli, F. 1978, *A&A* 69, 22
- Castelli, F., & Kurucz, R. L. 2004, arXiv:astro-ph/0405087
- Chadima, P., Harmanec, P., Bennett, P. D. et al. 2011, *A&A* 530, A146
- Chadima, P., Harmanec, P., Yang, S., et al. 2010, *IBVS* 5937
- Chaffee, F. H. & White, R. E. 1982, *ApJS* 50, 169
- Ekstrom S., Georgy C., Eggenberger P. et al. 2012, *A&A* 537, A146
- Ferluga, S., & Mangiacapra, D. 1991, *A&A*, 243, 230
- Geise, K. M., Stencel, R. E., Manset, N., Harrington, D., Kuhn, J. 2012, *J. AAVSO Vol.* 40, 767
- Granzer, T., Reegen, P., & Strassmeier, K. G. 2001, *AN* 322, 325
- Granzer, T., Weber, M., & Strassmeier, K. G. 2010, *Adv. in Astr.* 2010, ID 980182
- Gray, D. F. 2005, *The observation and analysis of stellar photospheres*, 3rd ed., Cambridge University Press
- Griffin, R. E., & Stencel, R. E. 2013, *PASP* 125, 775
- Guinan, E. F., Mayer, P., Harmanec, P. et al. 2012, *A&A* 546, A123
- Gustafsson, B., Edvardsson, B., Eriksson, K., Jørgensen, U. G., Nordlund, A., & Plez, B. 2008, *A&A* 486, 951
- Hack, M. 1959, *ApJ* 129, 291
- Harmanec, P., Bozic, H., Korcakova, D. et al. 2013, *Cent. Eur. Astrophys. Bull.* 37, 99
- Harrington, D. M., & Kuhn, J. R. 2009, *ApJS* 180, 138
- Heintz, W. D. & Cantor, B. A. 1994, *PASP* 106, 363
- Hog, E., Fabricius, C., Makarov, V. V. et al. 2000, *A&A* 355, L27
- Hoard, D. W., Ladjal, D., Stencel, R. E., & Howell, S. B. 2012, *ApJ* 748, L28
- Kawka, A., & Vennes, S. 2012, *MNRAS* 425, 1394
- Kim, H. 2008, *JASS* 25, 1
- Kloppenborg, B., Stencel, R., Monnier, J.D. et al. 2010, *Nature* 464, 870
- Kloppenborg, B., Hopkins, J. L., & Stencel, R. 2012, *JAAVSO* 40, 1
- Kolláth, Z. 1990, *Occasional. Technical Notes of Konkoly Obs.*, No. 1.
- Kolláth, Z., & Oláh, K. 2009, *A&A* 501, 695
- Kovtyukh, V. V., Gorlova, N. I., & Belik, S. I. 2012, *MNRAS* 423, 3268
- Kupka, F., Dubernet, M.-L. et al. 2011, *Baltic Astronomy* 20, 503
- Lambert, D. L. & Sawyer, S. R. 1986, *PASP* 98, 389
- Leadbeater, R., & Stencel, R. 2010, arxiv.org/abs/1003.3617
- Leadbeater, R., Buil, C., Garrel, T. et al. 2012, *J. Amer. Assoc. Var. Star Obs.* 40, 729
- Lenz, P., & Breger, M. 2005, *Comm. Asteroseismology* 146, 53
- Lucy, L. B. 1976, *ApJ* 206, 499
- Ludendorff, H. 1903, *AN* 164, 81
- Lutz, T. E., & Lutz, J. H. 1977, *AJ* 82, 431
- Martins, F., & Palacios, A. 2013, *A&A* 560, 16
- Meszaros, Sz., Dupree, A. K., & Szalai, T. 2009, *AJ* 137, 4282
- Mourard, D., Harmanec, P., Stencel, R. et al. 2012, *A&A* 544, A91
- Münch, G. 1957, *ApJ* 125, 42
- Pavlenko, Ya. V., & Magazzú, A. 1996, *A&A* 311, 961
- Petrie, R. M. 1966, in K. Loden, L.O. Loden, & U. Sinnerstand (eds.), *IAU Symp.* 24, Academic Press London, p.304
- Potravnov, I. S., & Grinin, V. P. 2013, *Astronomy Reports* 57, 991
- Reese, D. R., Prat, V., Barban, C., van 't Veer-Menneret, C., & MacGregor, K. B. 2013, *A&A* 550, A77
- Richichi, A., & Roccatagliata, V. 2005, *A&A*, 433, 305
- Royer, F., Grenier, S., Baylac, M.-O., Gómez, A. E., & Zorec, J. 2002, *A&A* 393, 897
- Sadakane, K., Kambe, E., Sato, B., Honda, S. & Hashimoto, O. 2010, *PASJ* 62, 1381
- Saito, M., Kawabata, S., Saijo, K. & Sato, H. 1987, *PASJ* 39, 135
- Schaller G., Schaerer D., Meynet G., Maeder A. 1992, *A&AS* 96, 269
- Schanne, L. 2007, *IBVS* 5747
- Stefanik, R. P., Torres, G., Lovegrove, J., et al. 2010, *AJ* 139, 1254
- Stencel, R. E. 2012, *J. Amer. Assoc. Var. Star Obs.* 40, 618
- Stencel, R. E. 2013, *Cent. Eur. Astrophys. Bull.* 37, 85
- Stencel, R. E., Kloppenborg, B. K., Wall, R. E. et al. 2011, *AJ* 142, 174
- Strassmeier, K. G., Boyd, L. J., Epan, D. H., & Granzer, T. 1997, *PASP* 109, 697
- Strassmeier, K. G., & Fekel, F. C. 1990, *A&A* 230, 389
- Strassmeier, K. G., Granzer, T., Weber, M., et al. 2004, *AN* 325, 527
- Strassmeier, K. G., Granzer, T., & Weber, M. 2010, *Adv. in Astr.* 2010, ID 970306
- Strassmeier, K. G., Reegen, P., & Granzer, T. 2001, *AN* 322, 115
- Strassmeier, K. G., Weber, M., Granzer, T., & Järvinen, S. 2012, *AN* 333, 663
- Struve, O., Pillans, H. & Zebergs, V. 1958, *ApJ* 128, 287
- Telting, J. H. 2013, <http://www.not.iac.es/instruments/fies/>
- van de Kamp, P. 1978, *AJ* 83, 975
- van Leeuwen, F. 2007, *A&A* 474, 653
- Vogel, H. C. 1903, *ApJ* 17, 243
- Wallace, L., Hinkle, K. & Livingston, W. 1993, *NSO Tech. Rep.* 93-001
- Wallerstein, G., Sandstrom, K., & Gredel, R. 2007, *PASP* 119, 1268
- Weber, M., Granzer, T., Strassmeier, K. G., & Woche, M. 2011, *Proc. SPIE* 7019, 70190L
- Weber, M., Granzer, T., Strassmeier, K. G., & Woche, M. 2012, *Proc. SPIE* 8451, 8451-19
- Wilson, R. E. 1971, *ApJ* 170, 529
- Wolk, S. J., Pillitteri, I., Guinan, E., & Stencel, R. 2010, *AJ* 140, 595

A The optical spectrum of ϵ Aur

B Spectral line identifications

C Line traces during eclipse

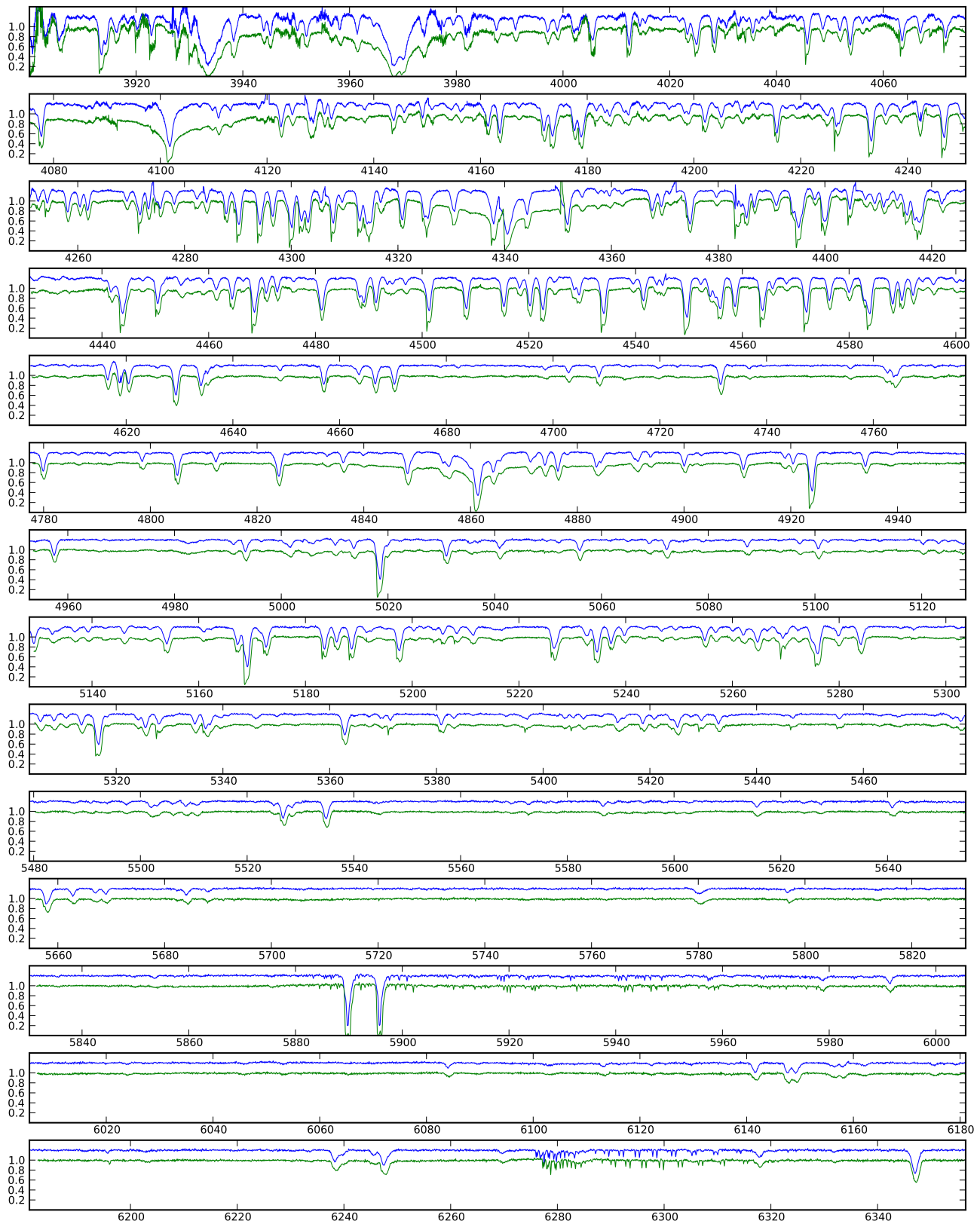


Fig. A1 The optical spectrum of ϵ Aur. The top spectrum is from outside eclipse and was taken January 9, 2008 (HJD 2,454,474.509) and is shifted arbitrarily by 0.2 in intensity. The bottom spectrum was taken September 4, 2011 (HJD 2,455,808.734) near the end of the dust eclipse and within the gaseous eclipse. Both spectra are shifted to the rest wavelength. The disk absorption appears as a strongly blue shifted asymmetry. Notice the extra ± 20 -Å line broadening of H α , H γ , H δ during eclipse, but not for H β .

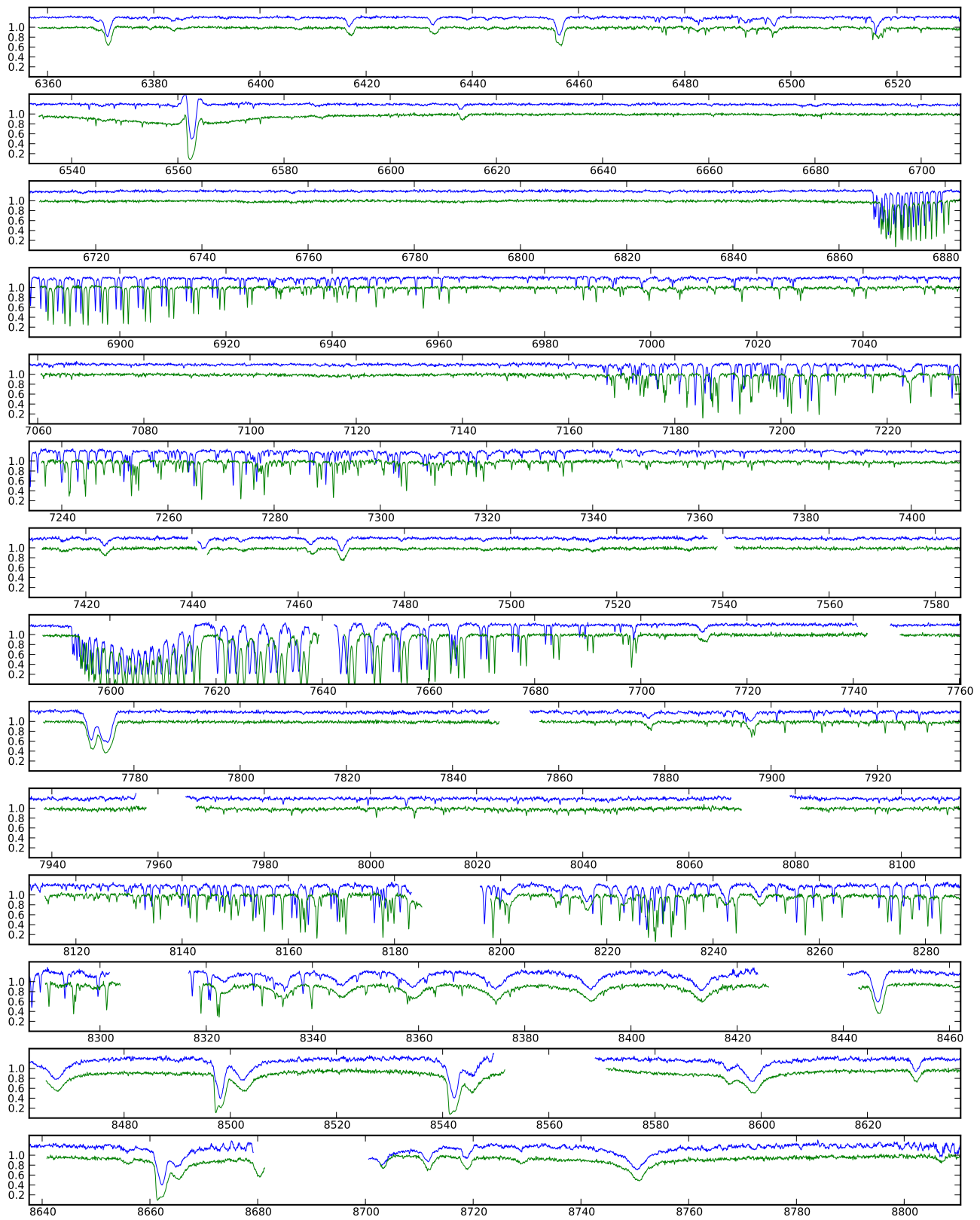


Fig. A2 (continued)

Table B1 Spectral lines without disk absorption during eclipse.

#	Line i.d.	#	Line i.d.	#	Line i.d.
1	Si I 3905.52	70	Ti II 4544.01	139	Fe I 5274.98 + Cr II
2	? + Fe I 3918.4 + Fe I 3918.65	71	Ti II 4545.14	140	Cr II 5279.9 + Cr II
3	Fe I 3925.95 + Fe I 3926.0	72	Ti II 4552.25	141	Cr II 5305.85
4	Ca II K 3933.7	73	Cr II 4558.66	142	Cr II 5308.4
5	Al I 3944.0	74	Ce II 4565.84	143	Cr II 5310.7
6	Ca I 3948.9	75	Ti II 4568.31	144	Cr II 5313.6
7	Y II 3950.3	76	Fe II 4576.33	145	Fe I 5324.18
8	Ca II H 3968.5	77	Fe II 4582.84	146	Fe II 5325.6
9	Co I 3979.5 + Fe I 3979.6	78	Cr II 4588.22	147	Cr II 5334.9
10	Cr I 3983.9 + Fe I 3983.95	79	Ti II 4589.96	148	Ti II 5336.81
11	Zr II 3991.1	80	Cr II 4592.09	149	Fe I 5383.35
12	Fe II 4002.1	81	Ce II 4593.93 + Cr I	150	Fe I 5404.15 + Fe I
13	Fe I 4014.28	82	Fe I 4596.060	151	Cr II 5407.6
14	V II 4023.39	83	Cr II 4616.64	152	Fe II 5414.1
15	Fe I 4029.64	84	Cr II 4618.83	153	Fe I 5415.20
16	Mn I 4048.74 + Cr I 4048.78 + Fe II	85	Fe II 4620.51	154	Fe II 5425.3
17	Fe I 4051.92	86	Cr II 4634.11	155	Fe II 5427.8
18	Mg I 4057.5 + Fe I blend + Fe II	87	Fe II 4635.32	156	Y II 5497.4 + Fe I 5497
19	Fe I 4067.0 + Cr I	88	Fe II 4656.981	157	Cr II 5502.1
20	Cr I 4111.0 + Cr II 4111.0	89	Fe II 4663.70	158	Cr II 5508.6
21	Fe II 4124.79	90	Fe II 4666.75	159	Fe II 5510.78
22	Si II 4128.05	91	Sc II 4670.4	160	Fe I 5572.84
23	Fe II 4128.74	92	Mg I 4702.98	161	Fe I 5586.75
24	Si II 4130.88	93	Ni I 4703.8	162	Fe I 5615.64
25	Fe I 4146.07	94	Ti II 4708.66	163	Fe I 5624.5
26	Fe I 4149.365	95	Fe II 4731.43	164	Fe II 5627.5
27	Cr II 4151.00	96	Ti II 4762.85 + Mn I 4762.37	165	Fe I 5662.51
28	Cr I 4161.52	97	C II 4771.67 + C I + Fe I	166	Na I 5688.20
29	Ti II 4163.64	98	Ti II 4779.98	167	Fe I 5780.600
30	Fe I 4172.13	99	Ti II 4798.53	168	Ti I 5797.4 + La II (?)
31	Fe I 4177.59	100	Ti II 4805.10	169	Co I 5991.88
32	Fe I 4181.76	101	Cr II 4812.36	170	Fe II 6084.1
33	Fe I 4203.95	102	Cr II 4824.13	171	Fe II 6113.32
34	Mn II 4205.37 + Eu II 4205.05	103	Cr II 4836.22	172	O I 6158.18
35	Fe I 4207.13	104	Cr II 4848.24	173	Fe I 6318.017
36	Zr II 4208.99	105	Sr I 4855.045	174	Si II 6347.1
37	Zr II 4211.88	106	Cr II 4864.3 + Ni I	175	Si II 6371.36
38	Sr II 4215.52	107	Ti II 4865.6	176	Fe II 6383.73
39	Fe I 4227.43	108	Ti II 4874.0	177	Ti II 6828.0 + C I/Fe I
40	Cr II 4242.38	109	Cr II 4876.41 + Cr II 4876.48	178	Si I 7425.95
41	Fe I 4250.79 + Fe I 4250.12	110	Y II 4883.69 + V II blend	179	N I 7423.64
42	Cr II 4252.63	111	Cr II 4884.6	180	N I 7468.31
43	Fe I 4258.32	112	Fe I 4890.75	181	O I 7772.0
44	Sr II 4305.45 + Fe I 4305.45	113	Fe I 4891.49	182	O I 7774.3
45	Sc II 4305.7	114	Fe II 4893.8	183	O I 7775.4
46	Y II 4309.62	115	Y II 4900.10 + Ti I 4899.91 + Ba II	184	N I 8216.3
47	Cr I 4344.51	116	Ti II 4911.15	185	Ca II 8248.8
48	Sc II 4354.61	117	Fe I 4918.99	186	Pa30 8287.6
49	Zr II 4379.78	118	Fe I 4920.50	187	Pa29 8292.4
50	Y II 4398.02	119	Ba II 4934.09	188	Pa28 8298.9
51	Fe I 4407.71	120	Fe I 4957.5 blend	189	Pa25 8323.3
52	Ti II 4411.08	121	Fe II 4993.3	190	Pa24 8334.5
53	Fe II 4413.60	122	Fe I 5056.0 + Si II 5055.98	191	Pa23 8345.8
54	Ti II 4441.73	123	Fe I 5068.76	192	Pa22 8359.0
55	Ca I 4454.78	124	Fe I 5072.67	193	Pa21 8374.8
56	Fe I 4461.66 + Zr II + Fe I blend	125	K I 5097.17 + Cr II 5097.3	194	Pa20 8392.4
57	Fe I 4466.55	126	Fe II 5100.95	195	Pa19 8413.3
58	Ti II 4470.86	127	Ti I 5120.415	196	O I 8446.4 + O I 8446.8
59	Fe II 4472.92	128	Y II 5123.2	197	Pa17 8467.3
60	Fe I 4476.02 + Fe I 4476.1	129	Fe II 5132.65	198	Pa16 8502.6
61	Mg II 4481.12 + Mg II 4481.3	130	Fe II 5136.8 + Ni I 5137.1 + Fe I	199	Pa15 8545.5
62	Ti II 4488.32	131	Fe I 5139.2 + Fe I 5139.5	200	? 8594.0
63	Fe II 4489.19	132	Fe II 5146.1	201	Pa14 8598.5
64	Fe II 4491.40	133	Fe I 5150.8	202	N I 8629.3
65	Ti II 4493.53	134	Fe I 5232.940	203	Pa13 8665.2
66	Fe I 4494.57	135	Fe II 5256.9	204	Si I 8680.2 + S I + S I
67	Zr II 4496.97	136	Ca I 5262.24 + Ti II 5262.1	205	N I 8711.7
68	Cr II 4539.62	137	Fe II 5264.8	206	N I 8718.8
69	Fe II 4541.52	138	Fe I 5266.5	207	Pa12 8750.6

Table B2 Spectral lines with disk absorption during eclipse.

#	Line i.d.	#	Line i.d.	#	Line i.d.
1	Fe I 3886.3	55	Mg I 4341.91	109	Fe II 5234.6
2	Fe I 3887.0	56	Mn I 4374.95	110	Cr II 5237.3
3	H8 3889.1 + Ca I	57	Fe II 4384.33	111	Sc II 5239.8
4	Fe I 3895.65 blend	58	Fe II 4385.39	112	Fe I 5254.95 + Cr I
5	Fe I 3899.7	59	Ti II 4386.86	113	Fe I 5269.5
6	Ti II 3900.55	60	Ti II 4394.06	114	Fe II 5276.00
7	Fe I 3902.95 blend	61	Ti II 4395.03 + Ti II 4395.85	115	Fe I 5284.42
8	Ti II 3913.45 + Fe I 3913.6	62	Sc II 4400.35	116	Fe II 5316.784
9	Fe I 3920.25	63	Fe I 4404.75	117	Fe I 5328.04 + Cr I 5328.36
10	? + Fe I 3922.9	64	Ti II 4409.25 + Ti II 4409.5	118	Fe II 5362.8
11	Fe I 3927.9	65	Fe I 4415.1	119	Fe I 5371.49
12	Fe I 3930.3	66	Sc II 4415.55	120	Ti II 5381.01
13	Fe II 3938.3 + Mg I 3938.4	67	Fe II 4416.81	121	Fe I 5383.35
14	V II 3951.95	68	Ti II 4417.71	122	Fe I 5397.13
15	Al I 3961.5 v.wk.	69	Ti II 4418.34	123	Fe I 5405.77
16	He ϵ 3970.	70	Ti II 4443.80 + Ti II 4444.56	124	Ti II 5418.7
17	Fe I 3977.7	71	Ti II 4450.49	125	Fe I 5429.69 + Fe I blend
18	Ti II 3982.0 + Fe I/Ti I 3981.75	72	Fe I 4459.1 + Ni I	126	Fe I 5432.9
19	Ti II 3987.6	73	Ti II 4464.5 + Fe I + Mn I	127	Fe I 5434.52
20	Fe I 4005.25 + V II 4005.7	74	Ti II 4468.49	128	Fe I 5446.91
21	Ti II 4012.4	75	Ti II 4501.27	129	Fe I 5455.61
22	V II 4023.3	76	Fe II 4508.29	130	Sc II 5526.78
23	Fe I 4024.73	77	Fe II 4515.33	131	Fe II 5534.85
24	Ti II 4028.33	78	Fe I 4518.4 + ? i.d.	132	Sc II 5641.0
25	Fe I 4045.81	79	Fe II 4520.22	133	Sc II 5657.90
26	Ti II 4053.8 + Cr II 4054.05	80	Fe II 4522.63	134	Sc II 5667.1
27	Ti II 4056.2	81	Fe I 4528.6 + 3 Fe I blends	135	Sc II 5669.0 v.wk. abs.
28	Fe I 4063.60	82	Ti II 4529.5 + Fe I 4529.55	136	Sc II 5684.2
29	Fe I 4071.74	83	Ti II 4533.97	137	Ba II 5853.7
30	Sr II 4077.71	84	Ti II 4549.63	138	Na I D 5889.95
31	H δ 4101.74	85	Fe II 4555.89	139	Na I D 5895.92
32	Fe II 4122.7	86	Ti II 4563.76	140	Ba II 6141.7 + Fe I
33	Fe I 4132.06	87	Ti II 4571.97	141	Fe II 6147.8 + Fe I
34	Fe I 4143.87	88	Fe II 4583.83	142	Fe II 6149.24
35	Fe II 4173.45 + Ti II 4173.55	89	Fe II 4629.33	143	Ca I 6162.1
36	Fe II 4178.86 + Cr I 4179.43	90	H β 4861.33	144	Fe II 6238.37
37	Fe I 4202.03	91	Fe II 4923.92	145	Fe II 6247.6
38	Cr II + V II + 3 blends	92	Ti II 5013.7	146	Fe I 6416.93
39	Ca I 4226.72	93	Fe II 5018.43	147	Fe II 6432.68
40	Fe I 4227.4	94	Fe I 5031.04	148	Fe II 6456.37 + Ca II 6456.87
41	Fe II 4233.16	95	Si II 5041.026	149	Ba II 6496.90 + Fe I
42	Sc II 4246.82 + Fe I 4247.43	96	Ti II 5129.2	150	Fe II 6516.05 + Sc II 6516.13 + H ₂ O
43	Cr I 4254.34	97	Ti II 5154.1 + Co I	151	H α 6562.85
44	Ti II 4301.93	98	Mg I 5167.3 + Fe I 5167.49	152	Y II 6613.8 + Fe I 6613.9
45	Fe II 4303.18	99	Fe II 5169.1 + Fe I 5169.30	153	Cr I 7462.35
46	Ti II 4307.90	100	Mg I 5172.7	154	K I 7664,7698.96
47	Ti II 4312.86	101	Mg I 5183.60	155	Fe II 7711.71 + Sm II 7712.04(?) + H ₂ O
48	Ti II 4314.98	102	Ti II 5185.9	156	O I 8446.76
49	Ti II 4316.80	103	Ti II 5188.7 + Ca I 5188.848	157	Ca II 8498.2
50	Na II 4320.91	104	Fe II 5197.55	158	Ca II 8542.09
51	Fe I 4325.76	105	Cr I 5204.50 + Fe I	159	N I 8629.25 v.wk.abs
52	Ti II 4330.7	106	Cr I 5206.02	160	Ca II 8662.3
53	Ti II 4337.92	107	Cr I 5208.41	161	Mg I 8806.8
54	H γ 4340.47	108	Fe I 5227.15		

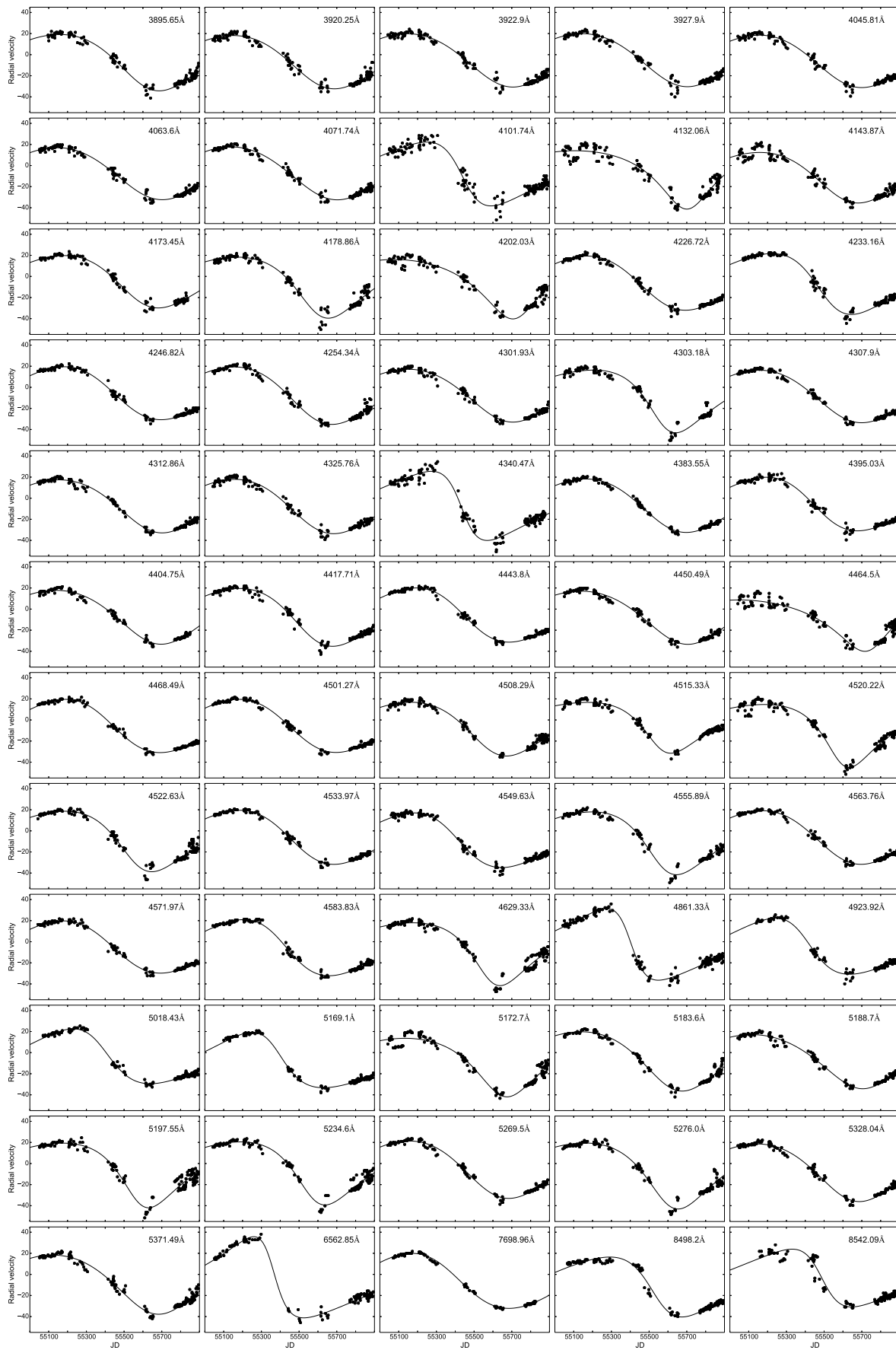


Fig. C1 Line traces for 60 spectral lines during eclipse. Each panel is for one spectral line and shows radial velocity of the disk absorption feature as a function of time in fractional JD24+. The wavelength of the line is indicated in each panel.